Simulating the Elastic Response of the Solid Earth due to Ocean Tide Loading in the La Plata Estuary

Thesis

Presented in Partial Fulfillment of the Requirements for the Degree Master of Science in the Graduate School of The Ohio State University

By

Michael Kevin Whaley

Graduate Program in Geodetic Science

The Ohio State University

2021

Thesis Committee

Dr. Mike Bevis, Advisor

Dr. C.K. Shum

Dr. Demian Gomez

Dr. Junyi Guo

## Abstract

Mass redistribution due to the ocean tides cause deformation of the Earth's surface termed ocean tide loading. A suite of gridded disk loads, together with a uniform ocean surface height, was used to simulate ocean tide loading displacements at the La Plata LPGS station in South America. The unit response method used in this study offered a convenient technique to assess the impacts of varying seismic Earth models, grid resolutions, and coastline resolutions, and provided a fast procedure for predicting 3D site displacements upon implementation of an ocean tide model. Large differences in simulated site displacements were found due to varying input model parameters and further used to guide improvements of the model. Comparison to the Ocean Tide Loading Provider program yielded maximum differences of approximately 1.22, 0.44, and 0.41 millimeters in the vertical, east, and north displacement components across the different Earth models and dates considered. Relative agreement between this model and the Ocean Tide Loading Provider shows a promising indication for future implementation. Findings in this study will aid in following developments of ocean tide loading models for the La Plata region, and provides a suitable framework for other surface loading studies on a global scale.

## Acknowledgments

First and foremost, I would like to thank the SMART scholarship and Naval Oceanographic Office for enabling my pursuance of a graduate degree. Thank you to my advisor, Dr. Mike Bevis, for introducing me to the field of geodesy and for many years of guidance. I thank Dr. C.K. Shum for his research assistance that allowed me to grasp the practical applications of ocean tide modeling much more readily, and Dr. Gomez for providing me with a vital depth of knowledge in the mapping side of geodesy that will stick with me for years to come. Thank you to Dr. Junyi Guo for the profound influence he has had on my graduate experience and scientific interests. As Richard Feynman said, "I learned very early the difference between knowing the name of something and knowing something". I learned a similar lesson through Dr. Guo's teachings. I thank the small, but incredibly welcoming and diverse group of students in the Geodetic Science program here at Ohio State. Finally, I would like to thank Hongzhi Yao, Peter Matheny, and Jason Otero-Torres for our interesting conversations and help through the past few years of coursework and research.

## Vita

2019……………………………………B.S. Environmental Engineering, The Ohio State University

2019 to present…………………………Graduate Researcher and SMART Scholar, School of Earth Sciences, The Ohio State University

## Fields of Study

Major Field: Geodetic Science

Table of Contents

List of Tables

List of Figures

# Chapter 1. Introduction

Ocean tide loading (OTL) is the periodic loading on Earth's surface due to the redistribution of water mass following the ocean tides. The surface deforms in response to the weight of overlying water, resulting in displacement of the sea floor and neighboring landmasses. With the advent of precise space geodetic techniques, and subsequent improved accuracy of ocean tide modeling in recent decades, OTL has garnered a renewed interest in the Earth science community. This is in part due to necessary removal, or isolation, of the OTL signal from sensitive geophysical measurements (e.g. Bos & Scherneck, 2013; Penna et al., 2008; Thomas et al., 2007; Van Dam, 2016). Such is the case with Global Navigation Satellite System (GNSS) observations, where OTL signals have shown to contribute vertical displacements up to 10 centimeters near certain coastlines (Scherneck, 2016). While the solid Earth tide varies rather predictably, the deformation caused by OTL is more complicated due to the dependence on local crustal properties (Farrell, 1972). Further compounding this complexity is the inaccuracy of global ocean tide models (OTM) near coastlines where shallow waters and interaction with landmass introduces a high degree of variability (Shum et al., 1997; Stammer et al., 2014).

The La Plata estuary (Rio de la Plata) off the coasts of Argentina and Uruguay spans approximately 35,000 km$^2$ with its drainage basin encompassing nearly a quarter of the continent. GNSS stations, co-located tide gauges, and the recently developed Argentine-

German Geodetic Observatory (AGGO) are located along the coastline, providing an array of geodetic instrumentation for a wide range of scientific investigations. The wealth of observations made in the region marks the La Plata estuary as a prime candidate for OTL studies (Figure 1). The shallow bathymetry combined with variable oceanic, atmospheric, and river forcing inputs ultimately result in complex hydrodynamics (Fossati & Piedra-Cueva, 2013). Currents are driven from the South Atlantic, where the large width of the estuary forms a tidal prism with the M2 lunar constituent having the greatest influence (Piedra-Cueva & Fossati, 2007). Despite low tidal ranges and the relatively small mass of the Rio de la Plata, geophysical observations in the region must account for OTL effects for the utmost accuracy.


Figure 1. Map of study site. Green triangle: location of La Plata LPGS station (LPS); purple circle: location of AGGO; red triangles: additional GPS station locations; grey circles; tide gauge locations; **black** arrow: direction towards Atlantic Ocean. Station locations retrieved from https://www.sonel.org/ with reference directed to Dow et al. (2009). Map projection: Mercator.

Richter et al. (2017) modeled the loading response at AGGO using both a regional and global tidal model with plans of validation and improvement upon further observations. Findings demonstrated that the open ocean dominated the OTL signal with little contribution from the estuary. In this study, the elastic response at the La Plata LPGS station (LPS) was simulated using a suite of disk loads in a gridded fashion. With an assumed constant tidal height of 1 m across the ocean surface, a sensitivity analysis on elastic calculations was carried out with varying key model inputs. Displacements in the vertical, east, and north directions at LPS (Latitude: -34.906746°, Longitude: -57.932210°) were estimated utilizing various seismic Earth models (EM), grid resolutions, and coastline resolutions. A station-specific influence matrix representing the responses to each 1 m thick tidal disk was constructed and further used to simulate realistic displacements with implementation of an OTM. Model comparisons to the widely used Ocean Tide Loading Provider developed by Bos and Scherneck (http://holt.oso.chalmers.se/loading/) were included to highlight rough approximations on the accuracy and limitations of the proposed framework. This study sets out to understand the impact of key model parameters to assist in future OTL modeling in the region. Findings from this study will also aid in the development of a convenient OTL framework that can presumably be adopted for any station.

# Chapter 2. Methods

## 2.1 Model Framework

OTL predictions are typically computed in the spatial domain by convolution of complex tidal heights obtained from OTMs and a load Green's function (LGF) based on the point mass concept (Farrell, 1972; Van Dam et al., 2003). The use of point loads is facilitated by modern OTMs where the surface mass distribution can be sampled at high resolutions (Bos & Scherneck, 2013). However, with disk geometries, the response is not singular at the center of the load which simplifies and offers flexibility in loading analyses (Bevis et al., 2016). OTL programs such as LoadDef also include disk factors in the LGFs at certain distances from the station as they have shown to assist in convergence of the infinite sums involved (Farrell, 1972; Martens et al., 2019). For the purpose of this study, disk loads were used uniformly throughout and only displacement LGFs were considered.

A loading disk implies uniform pressure across its surface and axial symmetry as outlined by Spada (2003), namely:

$$\sigma(\vartheta) = \rho \begin{cases} T, & 0 \leq \vartheta \leq \alpha \\ 0, & elsewhere \end{cases} \tag{1}$$

Where $\sigma(\vartheta)$ is the loading function of mass per unit surface area, $\rho$ is the load mass density, $\vartheta$ describes the colatitude with respect to the pole (Z axis) of the disk, $\alpha$ is the angular radius of the disk expressed as a geocentric angle, and $T$ is the height or thickness of the disk. The load thickness is described in terms of an equivalent height of freshwater with density of 1000 $kg/m^3$. Equation 1 does not account for mass conservation: a load is added with no compensation elsewhere. Mass can be conserved in only 2 ways with disk loads, thus the loading function takes on different forms for uncompensated and compensated loads (Bevis et al., 2016; Spada, 2003). A schematic of the disk load problem is displayed in Figure 2.

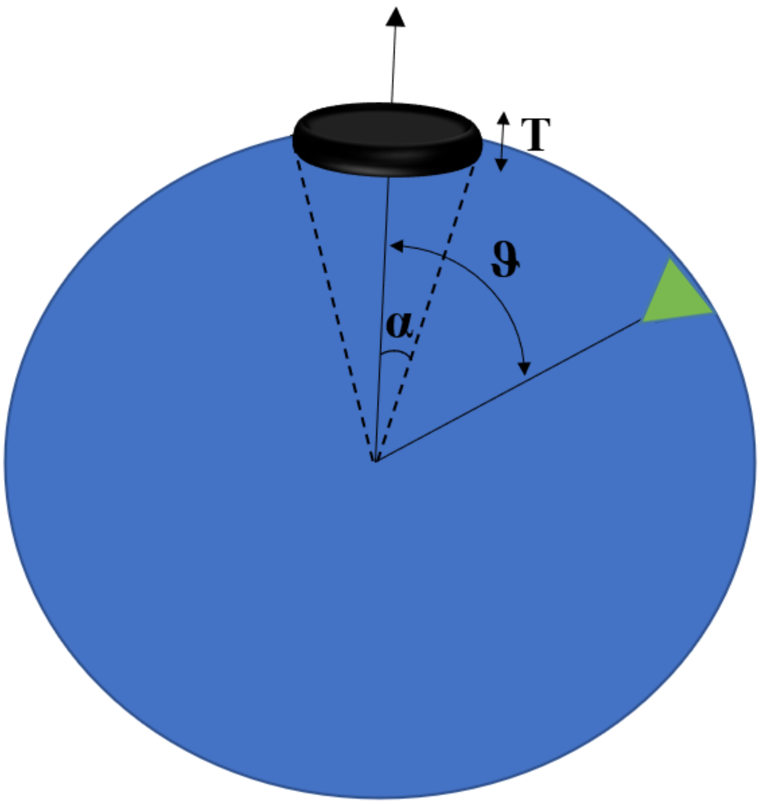


Figure 2. Simplified representation of a loading disk with accompanied geometric variables. Blue circle: spherical Earth representation; **black** disk; depiction of a single disk load; **green** triangle: station or point where displacements due to the loading disk are resolved; *T*: thickness of the disk; $\alpha$: angular radius of the disk; $\vartheta$: colatitude of station with respect to the disk pole.

The framework for this model follows similar studies in assuming the Earth as a layered, elastic, and self-gravitating sphere with a fluid core. Load Love number (LLN) formalism was naturally adopted with each set describing the elastic deformation of Earth's surface under loading. The LLNs, denoted as *h'* (vertical deformation), *l'* (horizontal deformation), *and k'* (gravitational potential), are derived from solving the equations of motion for a given EM. The specific weighted sums of the LLNs ultimately represent the LGF solutions expanded in a spherical coordinate system (Pan et al., 2015). The loading function is thus expanded in a series of Legendre polynomials with loading coefficients obtained for each degree *n* (Spada, 2003). Equations 2 and 3 show the formulation for load coefficients without mass conservation (uncompensated) and with mass conservation (compensated), respectively:

$$\sigma_n = \frac{\rho T}{2}\begin{cases}(1 - cos\alpha) & n = 0 \\ -P_{n+1}(cos\alpha) + P_{n-1}(cos\alpha) & n \geq 1\end{cases} \quad (2)$$

$$\sigma_n = \frac{\rho T}{2}\begin{cases}0 & n = 0 \\ \dfrac{-P_{n+1}(cos\alpha) + P_{n-1}(cos\alpha)}{1 + cos\alpha} & n \geq 1\end{cases} \quad (3)$$

Where $P_n$ represents the Legendre polynomial of degree *n*. The vertical (*U*) and horizontal (*V*) displacements are obtained in the local reference frame according to Equations 4 and 5:

$$U(\vartheta) = \frac{4\pi R_e^3}{M_e} \sum_{n=0}^{n_{max}} \frac{\sigma_n h'_n}{2n+1} P_n(cos\vartheta) \tag{4}$$

$$V(\vartheta) = \frac{4\pi R_e^3}{M_e} \sum_{n=1}^{n_{max}} \frac{\sigma_n l'_n}{2n+1} \frac{\partial P_n(cos\vartheta)}{\partial\vartheta} \tag{5}$$

$R_e$ and $M_e$ represent the spherical Earth's radius and mass, respectively. The radius of Earth used was $R_e$ = 6371 km along with $M_e$ = 5.963*$10^{24}$ kg. Vertical displacement is defined positive upwards and horizontal displacement is defined positive in the direction of increasing colatitude from the disk pole. In this way, a negative horizontal displacement at a station represents it moving "towards" the disk. Horizontal displacements are easily resolved into east and north components (Equation 6).

$$\begin{Bmatrix} E_i \\ N_i \end{Bmatrix} = V_i \begin{Bmatrix} sin\ Az_i \\ cos\ \ Az_i \end{Bmatrix} \tag{6}$$

Where *Az* represents the azimuth of the station from the pole of the $i^{th}$ disk.

LLNs were obtained for 3 different EMs: a variant of PREM (Pan et al., 2015) consisting of 56 mantle layers and 26 core layers which will be referred to as PREM, REF (Kustowski et al., 2008), and another modified version of PREM (Guo et al., 2004) hereafter referred to as MPREM. PREM and MPREM LLNs were given in a center of solid Earth frame (CE), while REF was obtained in a frame tied to the center of mass of the Earth

+ load system (CM). Conversion between frames involves modification to the degree 1 LLNs (Blewitt, 2003). For continuity, all EMs were considered in the CE frame with LLNs extrapolated up to $n$ = $10^5$ degrees using the ELLN software package (Chen et al., 2018). LLNs used in this study are plotted in Figure 3.

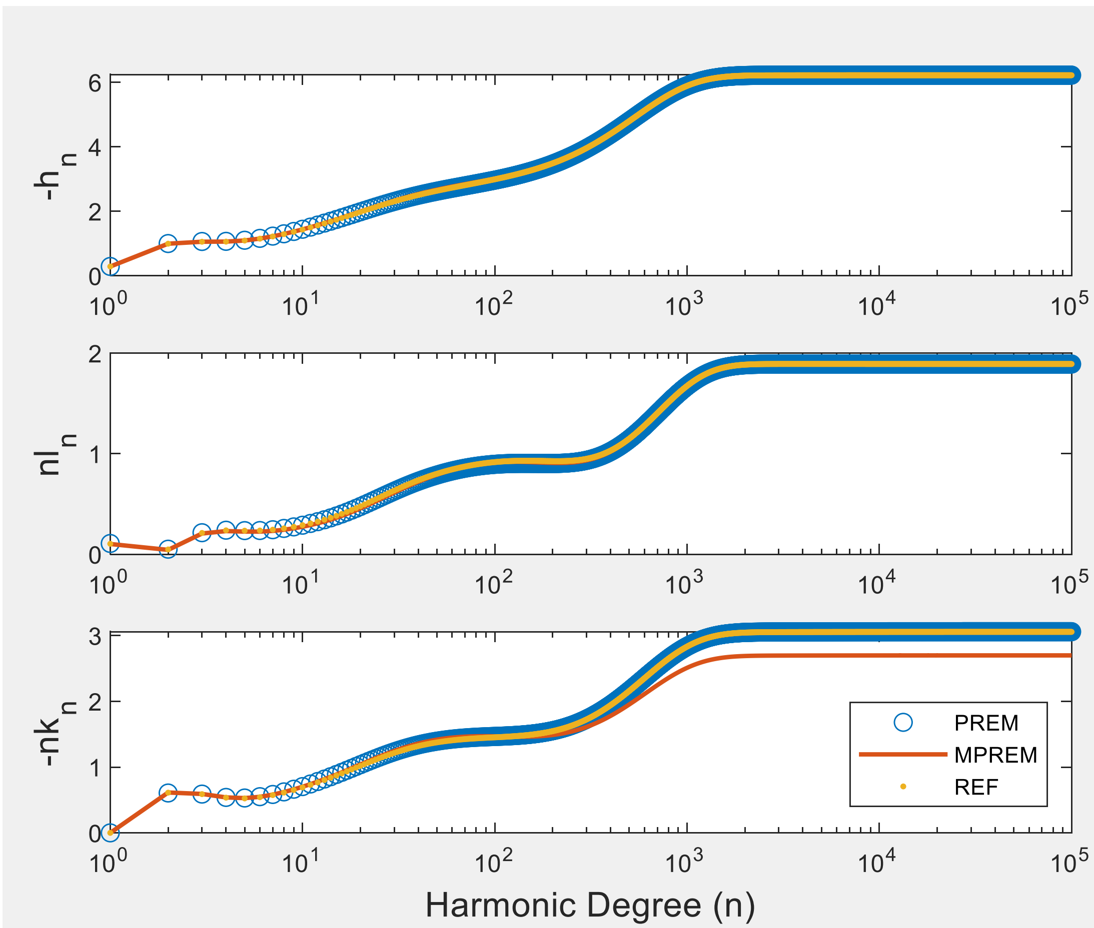


Figure 3. Load Love Numbers (LLN) expressed in the CE frame for the Earth Models PREM, MPREM, and REF for spherical harmonic degrees $n$ = 1 to $n$ = $10^5$. Note that degree 0 LLNs are not shown: the horizontal displacement ($l'_0$) and gravitational potential ($k'_0$) LLNs are both equal to 0 for all EMs. The degree 0 vertical displacement ($h'_0$) LLNs for PREM, MPREM, and REF read -0.13478, -0.13227 and -0.21600, respectively.

Effects of various inputs to the proposed model were analyzed by assuming a constant water height of 1 m across the ocean. Thus, the key idea behind the unit disk load model is the following: *given a grid covering the bodies of water on earth, each grid cell can be represented as a disk of water with constant thickness that imposes a load on Earth's surface.* Displacements in the *U*, *E*, and *N* directions due to each loading disk are resolved at LPS and stored in the so-called influence matrix. A summation of displacement components outturns the net unit response at LPS. Scaling the influence matrix by known tidal heights at each disk location can be used as an efficient method for predicting site displacements.

## 2.2 Gridding Scheme

Grids were constructed using the icosahedron pixelization of a sphere (Tegmark, 1996). This method is convenient due to the area equalization implementation and hexagonality of cells that best fit disk geometry. Equal area cells translate to uniform disk size, reducing computation time while also allowing for the use of splines for drastically improved calculation speeds. A spherical Voronoi tessellation of the Tegmark function output generates hexagonal grid cells of approximately equal area, where deviations in area are dealt with in terms of the load as discussed in Section 2.3.

One procedure used consistently across gridded surface loading studies is inclusion of a high-resolution grid near the stations of interest. This procedure is ideal for improved resolution where displacement effects are greatest and where the LGFs vary most rapidly. High-resolution cells are also necessary in OTL computations for accurate coastline fit to correctly represent the areas of tidal mass. The largest error sources in OTL predictions are attributed to errors in the OTMs followed by coastline representation and the convolution scheme (Bos & Baker, 2005; Francis & Mazzega, 1990; Penna et al., 2008). Local tide models and denser grids are used near the station to minimize these errors. OTL programs such as SPOTL (Agnew, 2012), LoadDef (Martens et al., 2019), and the Ocean Tide Loading Provider by Bos and Scherneck achieve higher resolution by subdividing cells or incrementing the mesh out from the station. These schemes are ultimately undesired here due to large changes in cell area which greatly impact the elastic calculation speeds. Given a restricted time frame, this gridding scheme must make a balanced trade-off between resolution and computational resources.

The number of pixels $N_p$ generated by the gridding function is determined by the input resolution parameter $R_p$ found in Equation 7 (Tegmark, 1996).

$$N_p = 40R_p\left(R_p - 1\right) + 12 \tag{7}$$

Initial tests showed that the spherical Voronoi tessellation required increasingly longer computational times with higher resolution inputs to the Tegmark function. A planar tessellation, although much faster, led to large area distortions and was deemed inadequate for scales larger than approximately 5° from LPS. Center points for a high-resolution grid (HR) were generated using the Tegmark function with $R_p = 500$, producing approximately $10^7$ pixels. Points out to a radial distance of 40° from LPS were extracted for cell generation; this distance is approximately where the LGFs briefly change sign from negative to positive and thus near where a maximum unit vertical response is expected. Extracting this subset also minimizes the number of cells passed into the time-consuming spherical tessellation program.

A total of $1.1675 \times 10^6$ cells were generated for the HR grid which required 209.13 hours. Large errors in cell areas were found on the outer edge of the grid due to the truncated spatial extent of points. The extent of the HR grid was thus reduced to approximately 39.9° to remove distorted cells from calculation. A lower resolution grid (LR) covering the entire globe was constructed with $R_p$ = 125 which represents 1/4 the resolution parameter used in the HR grid. In addition, another HR grid (HR2) extending 5° from LPS was produced with $R_p$ = 750 by implementing the planar tessellation. The HR2 grid was used to supplement investigations on load sizes in the near to medium fields of the station.

Grid cells covering ocean areas were determined using various resolutions of the Global Self-consistent, Hierarchical, High-resolution Geography Database file (Wessel & Smith, 1996). Both the high and coarse coastline resolutions were implemented separately for the HR grid. On the other hand, the HR2 grid was only intersected with the high-resolution coastline of South America due to not reaching any other continents. For the LR grid, the high-resolution coastline was used for South America and the coarse version for all other continents. It should be noted that coastline file for the boundary between Antarctica's ice and ocean was used throughout. For coastal cells, the fraction covering water was calculated by intersecting all cells with the coastline file. The fraction of each cell's water cover was used in computations in attempt to better represent the magnitude of the load. Cells thus possess a fraction of water equal to 0 (completely land), 1 (completely ocean), or a value in between (coastal). Grid cells greater than 10% water cover were considered for loading in efforts to capture a majority of the tidal mass with the limited grid resolutions.

Elastic calculations in this study used combinations of the HR+LR, HR2+LR, and only the LR grids. When multiple grids were used for the same computation, displacements from each grid were considered separately and then combined into the same influence matrix. Due to the gridding technique implemented, it was assumed that special care must be taken at the border between grids to accurately represent the ocean area. Masking out all LR cells within the bounds of the HR grid resulted in gaps of area between the two. Instead, LR cells within 0.1° of the HR border were included, ameliorating gaps but leading to areas of overlap (Figure 4). The same process was done for the HR2+LR grid combination. Overlapping areas were treated similar to coastal cells as discussed in Section 2.3. Note that the maximum extents of both the HR and HR2 grids were used in calculations unless stated otherwise.

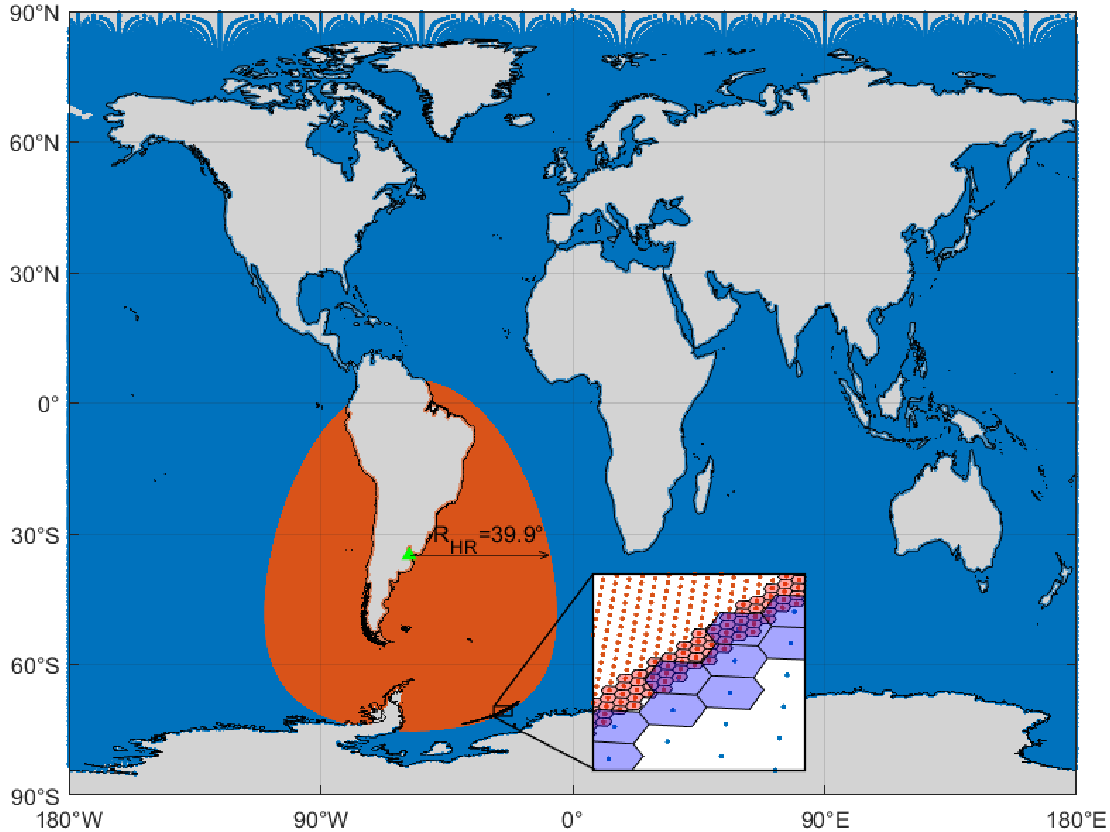

Figure 4. Oceanic and coastal grid centers plotted for the HR+LR grid combination. The zoomed in section explicitly shows grid cells to emphasize areas of overlap. Note that no projection was used to accommodate the magnified window. Green triangle: location of LPS; Orange area: HR grid points out to the maximum radial extent of 39.9048° from LPS; blue area: LR grid points extending from 0.1° inside the HR grid bounds out to 180° from LPS; grey areas: cells over continents that were not considered for OTL calculations.

### 2.3 Model Parameters

The elastic response at LPS was modeled following procedures outlined in Bevis et. al (2016). The provided diskload function returns the vertical and horizontal displacement components at a station due to parameterized loading disks. Input parameters are briefly described here for clarity on implementation. The angular radius α was calculated based on the mean cell area for each respective grid, giving way to 3 different angular radii that were used throughout. The maximum degree of expansion $N_{\text{max}}$ was set to $4 \times 10^4$ and later varied to analyze effects on the truncation degree. Angular distances $\vartheta$, or colatitudes, were calculated as the great circle arclengths from each disk center to LPS. The load parameter $w$ was set to 1 m to represent uniform tidal height across all cells. Table 1 summarizes key facets of each grid along with the parameters used in the function. The minimum degree of truncation is assumed to be 0.

| | HR Grid | HR2 Grid | LR Grid |
|---|---|---|---|
| Grid Attributes | | | |
| # of Total Cells | 1,167,455 | 42,751 | 620,012 |
| Max # of Loading Cells | 853,794 | 11,514 | 443,555 |
| Mean Cell Area ($km^2$) | 51.16 | 22.70 | 822.67 |
| Area Std. Deviation (km) | 0.2800 | 0.0126 | 0.8291 |
| Max Extent from LPS (°) | 39.905 | 4.93 | 180 |
| Coastline Intersects | 1. High<br>2. Coarse | 1. High (SA) | 1. High (SA) + Coarse elsewhere |
| Diskload Parameters | | | |
| α (°) | 0.0363 | 0.0242 | 0.1455 |
| *Nmax* | $4 \times 10^4 - 10^5$ | $4 \times 10^4 - 10^5$ | $4 \times 10^4 - 10^5$ |
| *Icomp* | 0 | 0 | 0 |
| *w* | 1 | 1 | 1 |

Table 1. Grid specifications and diskload function parameters used in this study. Note that the maximum number of loading cells for the LR grid is global, i.e., including all the ocean and coastal cells within the bounds of the HR grid. The term SA represents South America.

The parameter for mass compensation *icomp* requires special attention. It can be set to either 0 or 1 for uncompensated loads or compensated loads, respectively. The ocean tide conserves mass and therefore the physical model should as well. However, conservation of mass in this unit response model is futile at the given scale. A constant tidal height of 1 m is assumed over the ocean surface, a condition clearly unattainable by mass redistribution. Furthermore, compensation via the function is performed uniformly everywhere outside of the loading cell, i.e., including areas over land (Bevis et al., 2016). This leads to erroneous results by putting the station in the vicinity of negative mass. Mass conservation was thus neglected in the unit response calculations. Unavoidably, uncompensated mass leads to inclusion of the degree 0 loading term (Equation 2), implying strict radial displacement due to the average load over the Earth's surface. Effects of degree 0 were handled when simulating true displacements by conserving mass in the OTM.

Another parameter that warrants further discussion is the load thickness $w$ which was set equal to 1 m for all disks in the elastic calculations. This, however, does not account for the density of seawater versus freshwater, inhomogeneity amongst grid cells, or cells that are partially over land. To better represent the magnitude of the load, the displacements to due to each disk were scaled accordingly (Equation 8).

$$w_i = \frac{A_{h,i}}{A_d}\frac{\rho_s}{\rho_f} f_{w,i} \tag{8}$$

Where $i$ denotes the set of cells, $A_h$ is the cell area, $A_d$ is the disk area, $\rho_s$ and $\rho_f$ are the densities of seawater and freshwater, respectively, and $f_w$ is the cell fraction covering water. A constant seawater density of 1030 kg/m$^3$ was used throughout. Overlapping cell areas on the grid borders were treated as land by subtracting the overlapped area from $f_w$ of the LR cells.

Equation 8 scales the height of water by the ratio of the cell area to the disk area, supporting the use of constant disk sizes for each grid. Despite modest improvements in computational speed with constant disk sizes, the expansion up to $N_{max}$ for each of 1 million grid points remained costly. Constant angular radii for each grid more importantly allow for spline fitting to quickly evaluate loading responses. Splines were fit to the diskload function outputs $U$ and $V$ based upon the input EM, $\alpha$, $N_{max}$, and *icomp* parameters. The Legendre polynomial expansion is thus computed for various $\vartheta$ only once, providing up to 500 times faster computation depending on the number of points evaluated. Accuracy of spline results were evaluated using the EM PREM with $\alpha$ = 0.1455°, no mass compensation, and $N_{max}$ = 4 x $10^4$. Average percent errors in $U$ and $V$ were 8.7 x $10^{-4}$ and 7.26 x $10^{-4}$, respectively. The exceptional fit to expected outputs validated the use of spline evaluation for vastly reduced calculation time.

# Chapter 3. Results

## 3.1 Framework Validation

To validate the model framework, the model was run considering the Earth's surface as entirely ocean with an applied 1 m water load to all grid cells in the HR+LR grid combination. Upon conservation of mass the net displacement at any location should theoretically equal 0, i.e., a load is applied everywhere and equally compensated everywhere. Figure 5 highlights this case by showing the cumulative unit response displacements at LPS for the EM PREM.

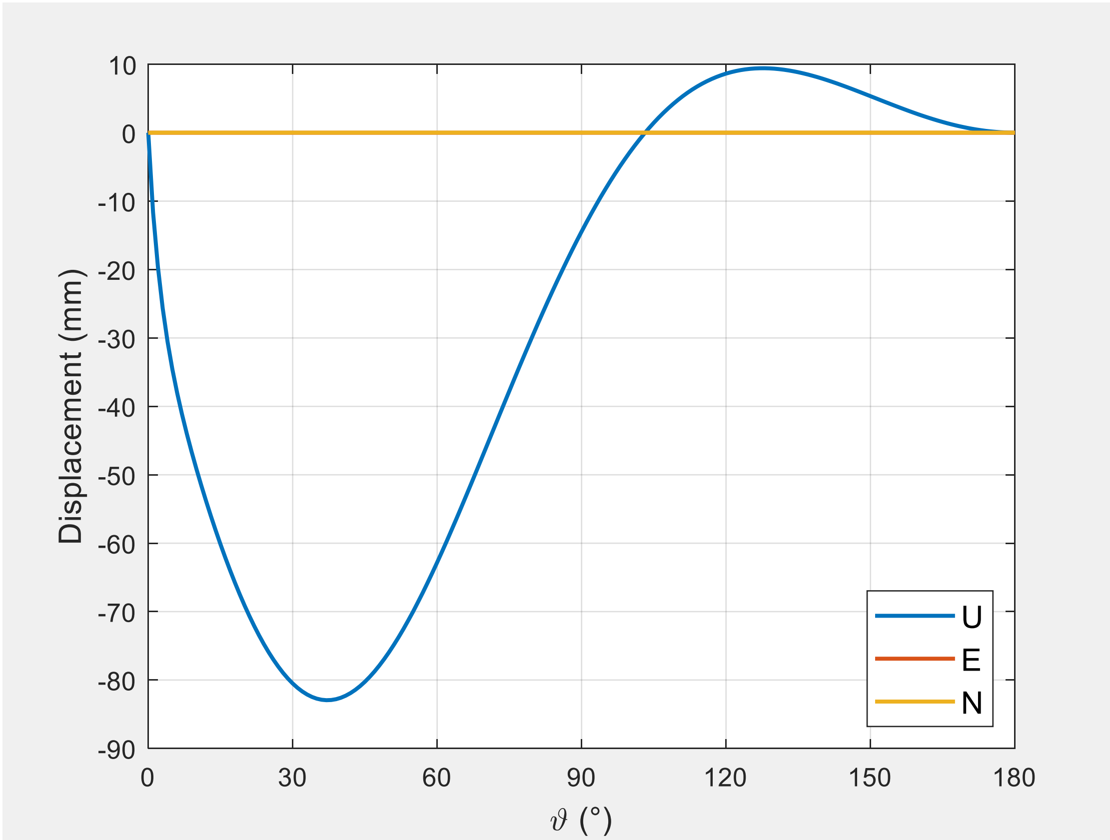

Figure 5. Cumulative unit response displacements at LPS on an idealized all-ocean world (no land masses) using the HR+LR grid combination and with mass conservation enforced. The EM PREM was implemented although similar results are achieved with all EMs.

A net vertical response of approximately 8.0 x $10^{-3}$ mm was obtained when summing contributions from all disks. A result slightly off from 0 is anticipated due to disk load geometries and minor errors in the total grid area. In contrast to this, an all-ocean Earth was assumed but without observance of mass conservation. Net vertical displacement then corresponds to the degree 0 LLN $h'_0$ as all other terms have been averaged out (Equation 9):

$$U = T_l \left(\frac{R_e}{M_e}\right) h_0' \tag{9}$$

Where $T_l$ is the total load over the entire surface in kg. Applying $h'_0$ for PREM, Equation 9 yielded a vertical displacement of -73.282 mm: approximately 0.17 mm off from the -73.450 mm obtained from the disk load model. Cumulative unit response displacements for the 3 EMs on the idealized all-ocean surface and with no mass conservation can be found in Appendix A. These tests highlight the accumulation of errors in the model framework thus far as well as the slight limitations of employing disk load geometries.

## 3.2 Earth Model Effect and Preliminary Findings

Vertical and horizontal displacements at LPS were computed with the EMs PREM, MPREM, and REF using the parameters discussed in section 2.3. The high-resolution coastline was initially used for the HR grid. Cumulative unit response displacements were plotted utilizing the HR+LR grid combination (Figure 6). Note that the idealized all-ocean surface is no longer assumed for the remainder of the study. This means Figure 6 resembles Figure 22 found in Appendix A except modified for the fact that landmasses are present on Earth's surface.

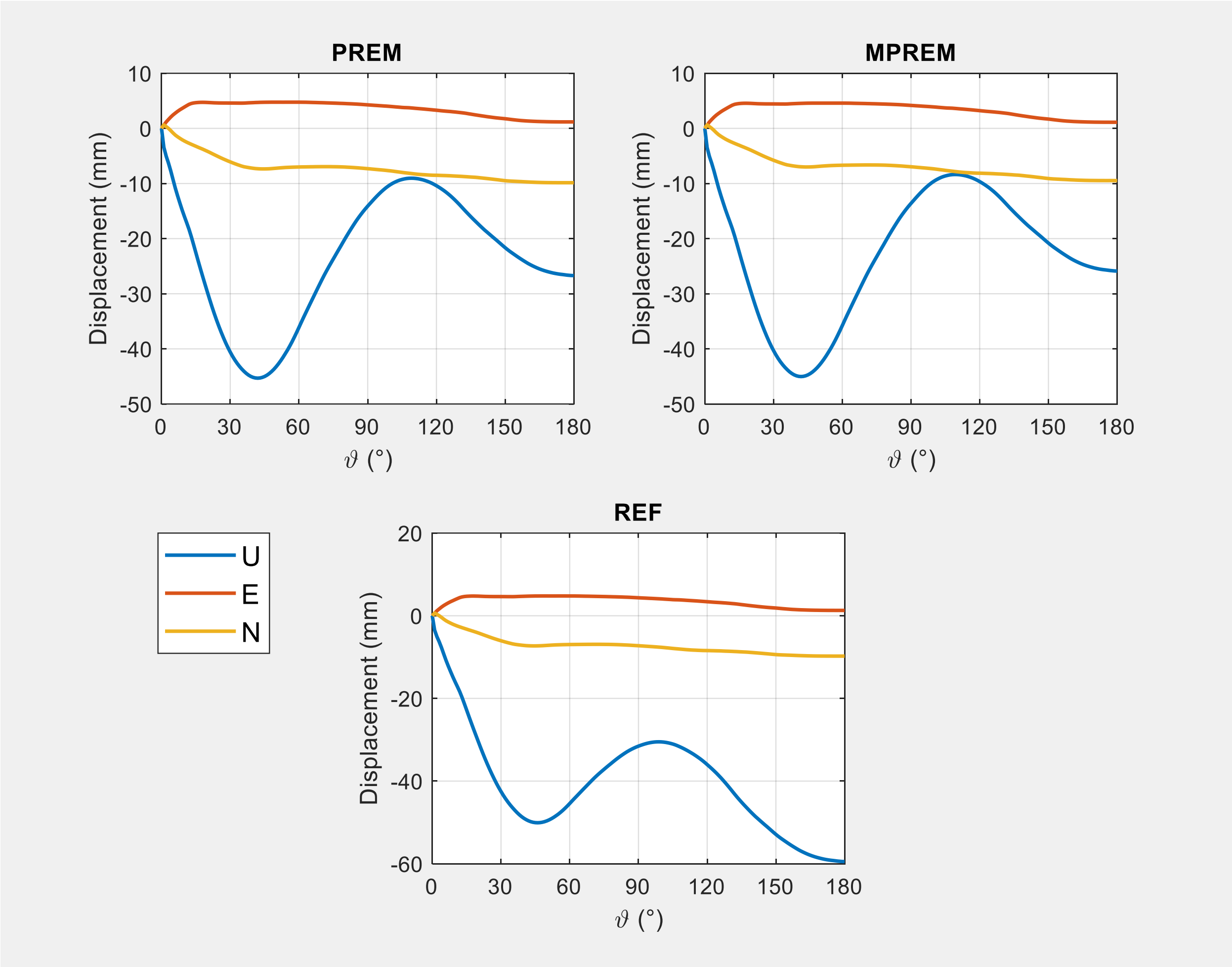

Figure 6. Cumulative unit response displacements at LPS utilizing the HR+LR grid combination for the EMs PREM, MPREM, and REF with no mass conservation. Total displacement at LPS represents the values attained at 180°.

Net displacements in *U*, *E*, and *N* are additionally displayed in Table 2 to highlight differences between the HR+LR and HR2+LR grid combinations. The large difference in net *U* displacement found between REF and the other EMs is primarily attributed to the stark differences in $h'_0$. Invoking mass conservation (*icomp*=1) brings the difference in *U* between PREM and REF to approximately 0.15 mm. Conserving mass in the unit response case is physically meaningless and brought to attention only to explain the large discrepancy. The contrast observed between PREM and MPREM results are predominately due to differences in the other spherical harmonic terms based upon the treatment of crustal layers and methods of LLN calculation (Guo et al., 2004; Pan et al., 2015).

Differences between the HR+LR and HR2+LR computations remained nearly constant across the EMs. The HR grid appeared to overestimate *E* displacements by approximately 0.03 mm, and underestimate *U* and *N* displacements by an average of 0.01 mm and 0.06 mm, respectively. This assumed that the HR2 grid is a more precise coastline fit. However, the radial extent of HR2 is much less than HR, putting the overlapping grid borders and LR cells closer to the station. Effects of overlapping cells with distance from LPS were explored further in Section 3.3. The rest of this study focuses on PREM under other varying model conditions.

| | PREM | MPREM | REF |
|---|---|---|---|
| **HR+ LR** | | | |
| U (mm) | -26.528 | -25.702 | -59.283 |
| E (mm) | 1.217 | 1.154 | 1.332 |
| N (mm) | -9.790 | -9.405 | -9.697 |
| **HR2+ LR** | | | |
| U (mm) | -26.537 | -25.710 | -59.305 |
| E (mm) | 1.182 | 1.121 | 1.297 |
| N (mm) | -9.846 | -9.459 | -9.753 |

Table 2. Net displacement results at LPS utilizing the EM's PREM, MPREM, and REF for the grid combinations HR+LR and HR2+LR.

Various types of surface loading phenomena pose impacts on different scales. Initial expectations reasoned that contributions from very distant disks would have little impact on the net result due to displacement LGFs decaying proportionally to the inverse distance from the station. Percent of net displacement was calculated at each 1° distance step in attempt to view the OTL in a regional sense. This is demonstrated with focus on the very far field using the HR+LR grid combination (Figure 7).

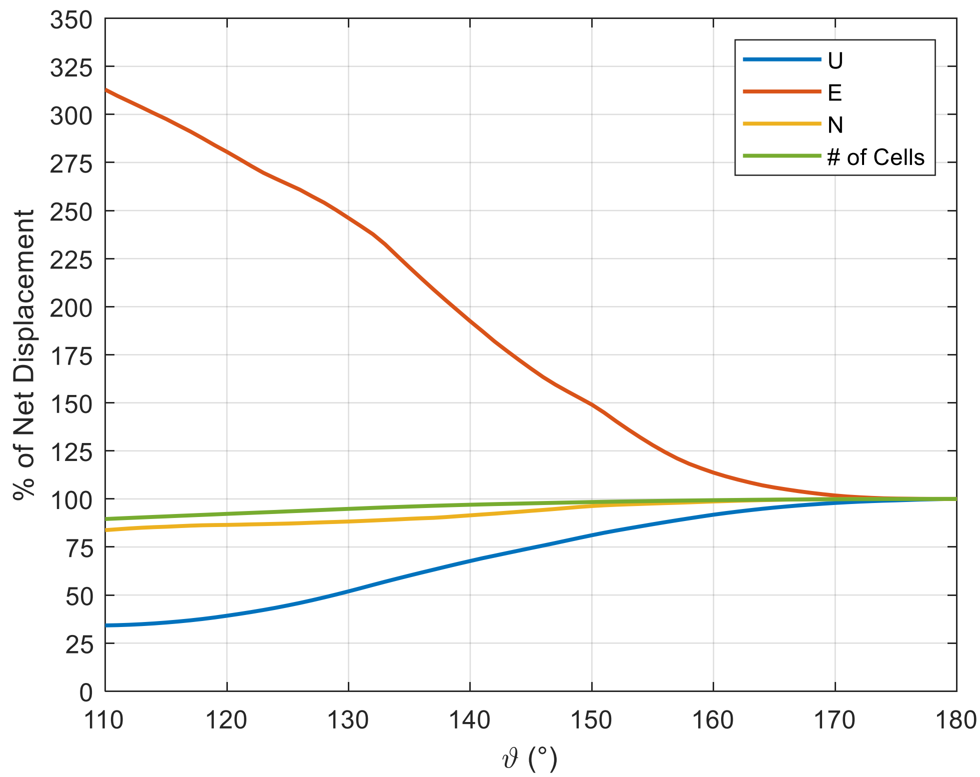


Figure 7. Percent of net displacement with increasing distance from LPS utilizing the HR+LR grid combination. Net displacement corresponds to summation of all disks out to 180°. Greater than 100% of net displacement represents changes in sign.

Despite the fact that 92% of disks were included at 120°, less than 50% of the final vertical displacement is achieved. Although the LGFs reach smaller magnitudes with increasing distance, the total mass of the ocean makes the sum of contributions from the far field significant. This example offers a practical perspective that OTL computations must consider the entire ocean domain rather than from the viewpoint of the mathematical theory.

Increasing the degree of truncation is achieved much more efficiently with adoption of splines. $N_{max}$ was varied from 4 x $10^4$ to $10^5$ to assess the sensitivity in vertical displacement (Figure 8). The HR+LR combination was used with the same $N_{max}$ for both the HR and LR computations despite different disk sizes. Figure 8 displays the results near 180° to show the differences in net displacement.

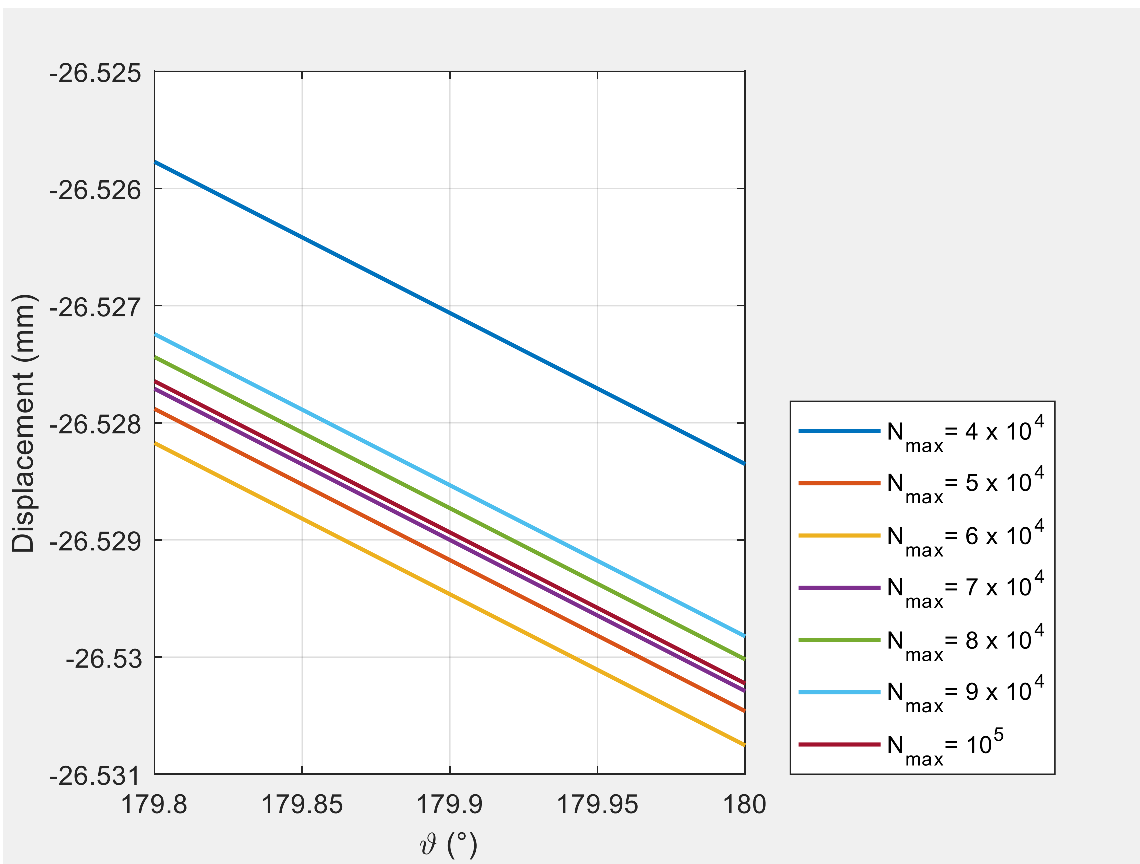


Figure 8. Impact on net displacement results with varying $N_{max}$. The rule of thumb presented in Bevis et al. (2016) lies at approximately $10^4$ for the HR grid, and approximately 2.5 x $10^3$ for the LR grid. $N_{max}$ = 4 x $10^4$ thus represents a safety factor of 4 for the HR grid.

Differences in $U$ were negligible at the degrees evaluated. Using $N_{max} = 10^5$ required 7.26 seconds to evaluate all spline responses which totaled 2.83 seconds longer than the time required for $N_{max} = 4 \times 10^4$. Lowering $N_{max}$ to $10^4$, which approximately follows the general rule presented in Bevis et al. (2016) for the HR disk size, led to a 0.01 mm difference when compared to $N_{max} = 4 \times 10^4$. Lower values can thus be used for quicker computation time although improvement on the order of seconds was of little concern here. The degree of truncation was kept to a constant $4 \times 10^4$ for the remainder of this study based on negligible differences in displacement and improvement in calculation speeds.

### 3.3 Effects of Load and Coastline Resolution

The load size, or grid resolution, has a significant impact on the accuracy of OTL results (Penna et al., 2008). Comparisons between the LR, HR+LR, and HR2+LR grids were done in an annulus fashion to investigate the effects of varying load resolution. The sum of 3D displacements from all cells greater than $\vartheta - 1°$ and less than or equal to $\vartheta$ from LPS were calculated for the 3 grid combinations. Differences between each annulus sum are displayed in Figures 9, 10, and 11. Note that these plots focus on small to medium distances from the station and thus represent differences between using the LR, HR, and HR2 resolutions in the near to medium fields.

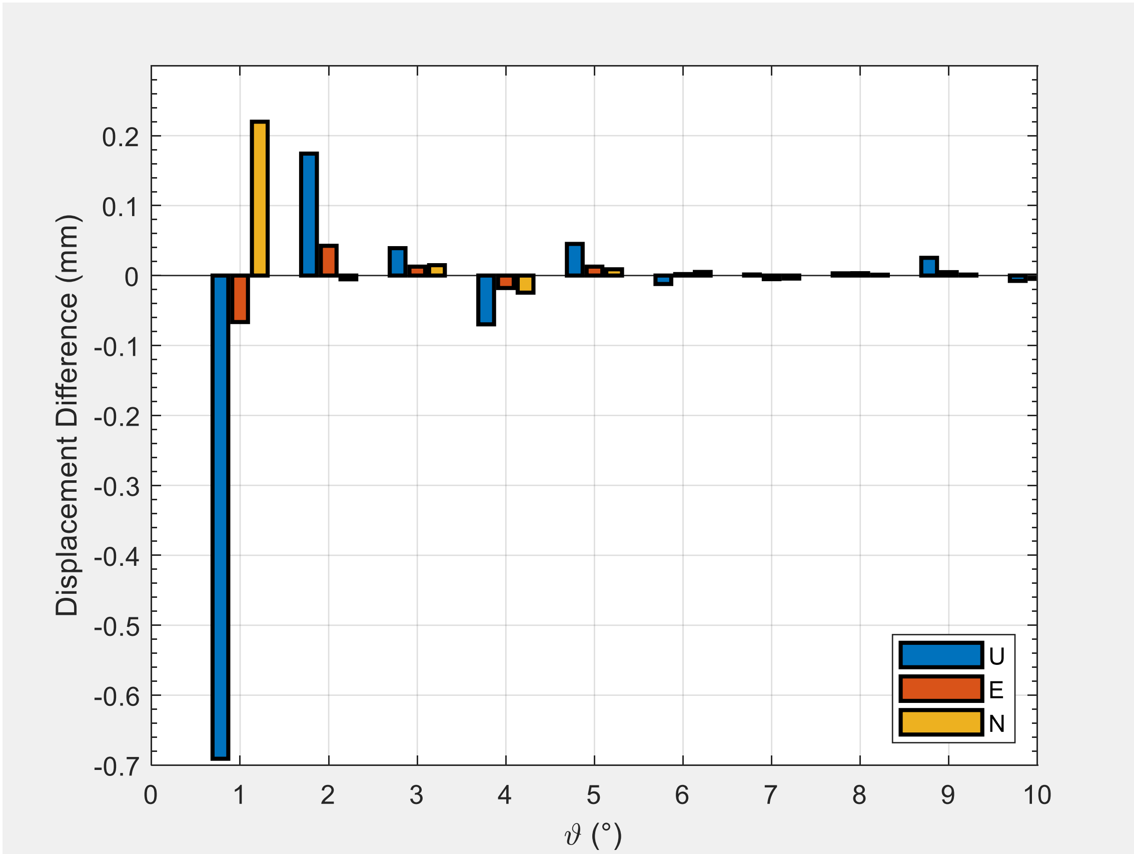

Figure 9. HR+LR annuli sums minus the LR annuli sums for each 1° step out to 10° from LPS.

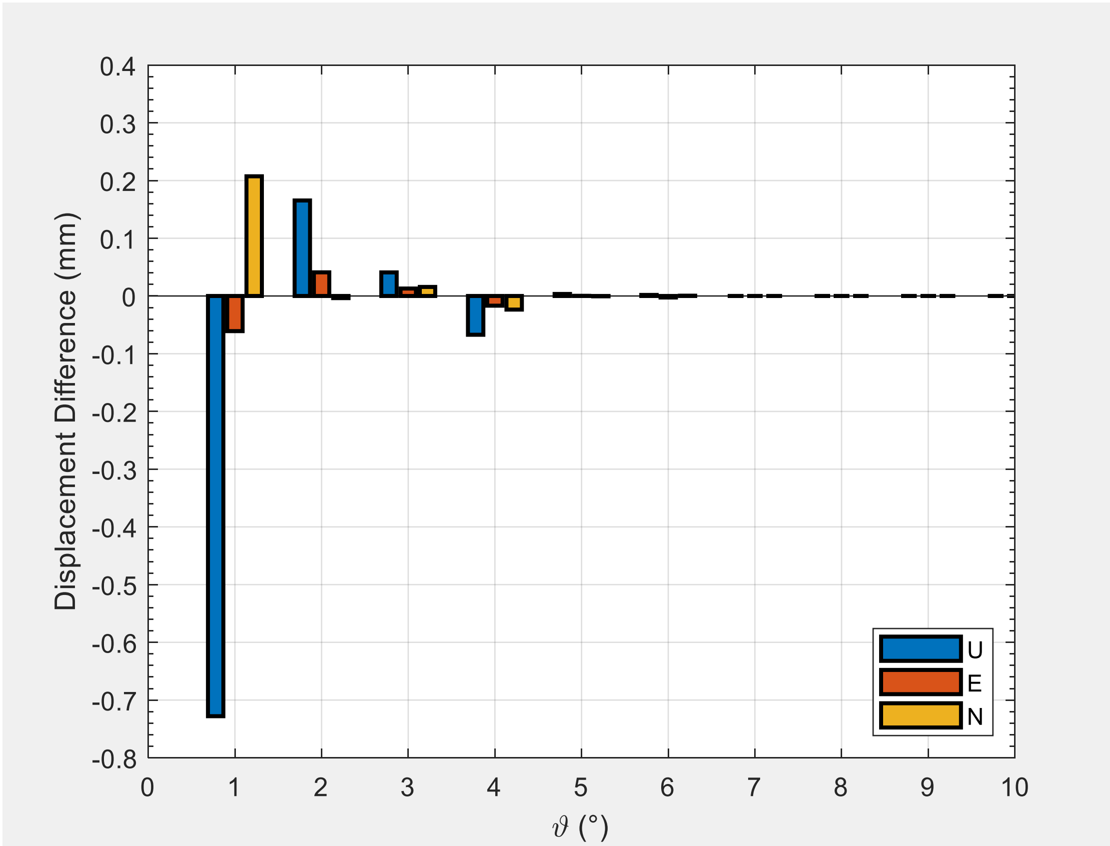


Figure 10. HR2+LR annuli sums minus the LR annuli sums for each 1° step out to 10° from LPS.

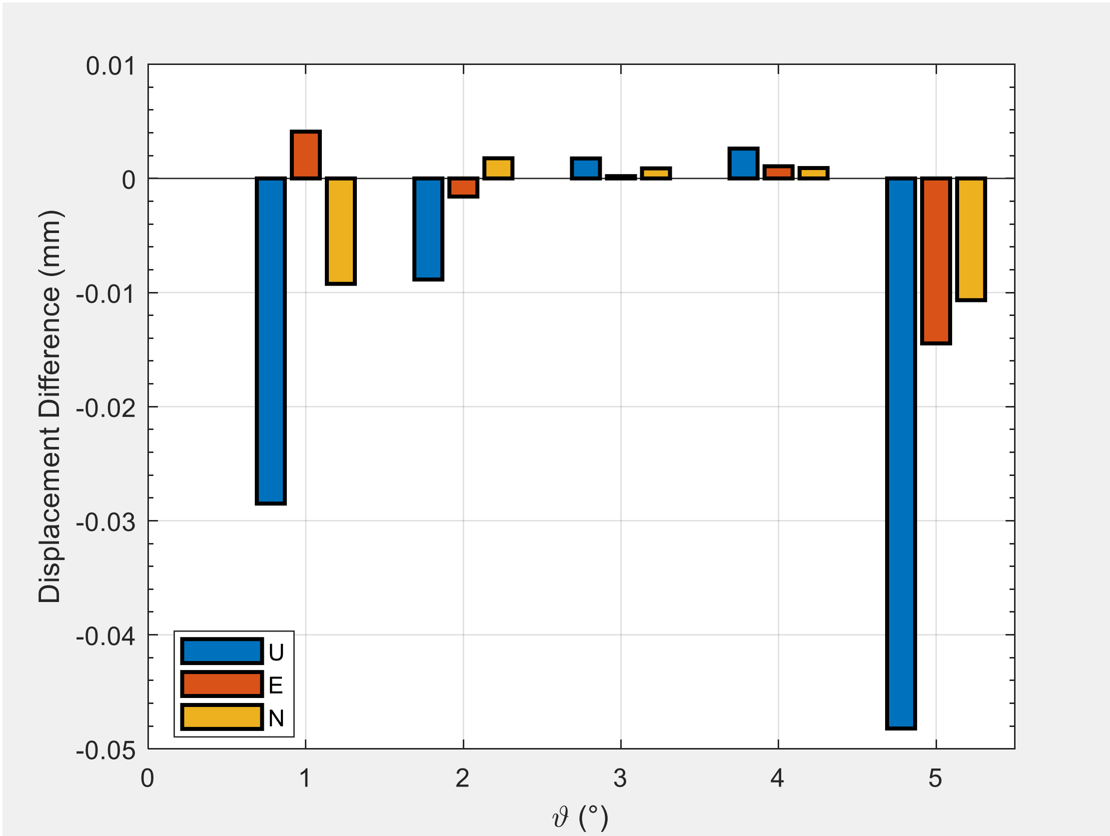

Figure 11. HR2+LR annuli sums minus the HR+LR annuli sums for each 1° step out to 5° from LPS. The plot is zoomed in farther to highlight differences between using the HR2 and HR resolutions close to the station.

Differences were strictly due to loading size as the same resolution of coastline for South America was implemented in all grids. Displacements using only the LR grid were either over or underestimated due to larger load sizes and, concomitantly, poor coastline fit. Using the LR grid in the near field placed LPS within a coastal disk, distorting the domain of tidal loading and explaining the large *U* discrepancy within 1° in Figures 9 and 10. The net differences between the HR+LR vs. LR computation amounted to -0.407, -0.030, and -0.216 mm for *U*, *E*, and *N*, respectively. Seeing as there were small differences after 5° for the HR+LR vs. LR grid (Figure 9), this may indicate that the HR2 grid needed to extend farther than 4.93° to minimize coastline errors. Negligible differences between the HR2+LR vs. LR calculations between 4° and 5° (where overlapping cells were present in the HR2+LR grid) highlights that treatment of overlapping border cells by the fraction of water cover ($f_w$) was indeed successful.

The negative difference at 1° for the HR2+LR vs. HR+LR calculations (Figure 11) showed that the HR grid accounted for slightly more water mass along the coastline due to inclusion of a coastal disk. These results suggests that scaling by $f_w$ to better represent the magnitude of the load is insufficient for small distances from the station. Net differences between the HR2+LR vs. HR+LR grids were identical to that shown in Table 2; the sum of all annuli differences out to 180° equals the difference in net displacements. For an additional test regarding near to medium field effects, the HR grid with the high-resolution coastline was contrasted with the coarse-resolution coastline (Figure 12). A total of 960 cells were excluded, or considered completely over land, and another 1249 cells showed a change in $f_w$ when implementing the coarse version. The number of oceanic and coastal cells were ultimately reduced which underestimated the tidal loading. This is not true for every region as a lower resolution coastline may either under or over fit the true coastline.

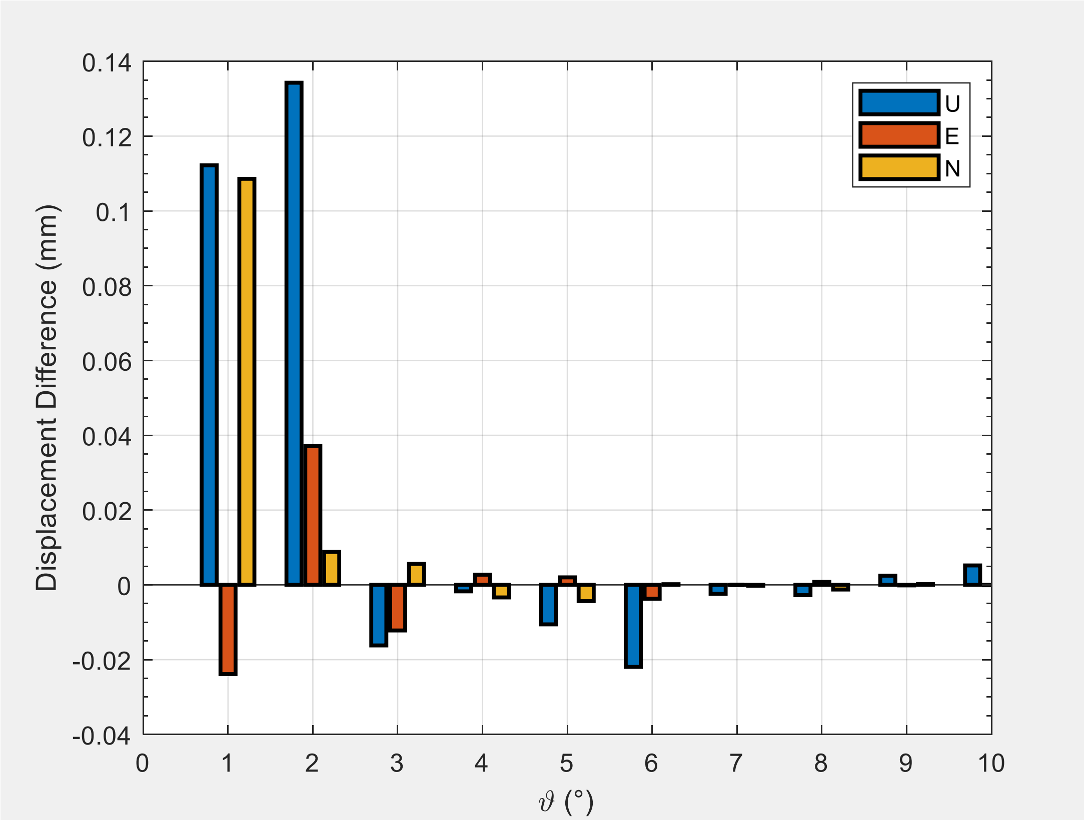

Figure 12. HR grid with the high-resolution coastline minus the HR grid with the coarse-resolution coastline annuli sums for each 1° step out to 10° from LPS.

Due to the limited extent of the HR2 grid, focus remained on the HR grid for analyzing effects at larger distances. The radial extent of the HR grid was varied from 5° to the original extent of 39.9° (Figure 13), offering possible insight to the optimal range of high-resolution cells for the region. Greater extents of the HR grid led to a greater number of overlapping cells on the border as more ocean area was included.

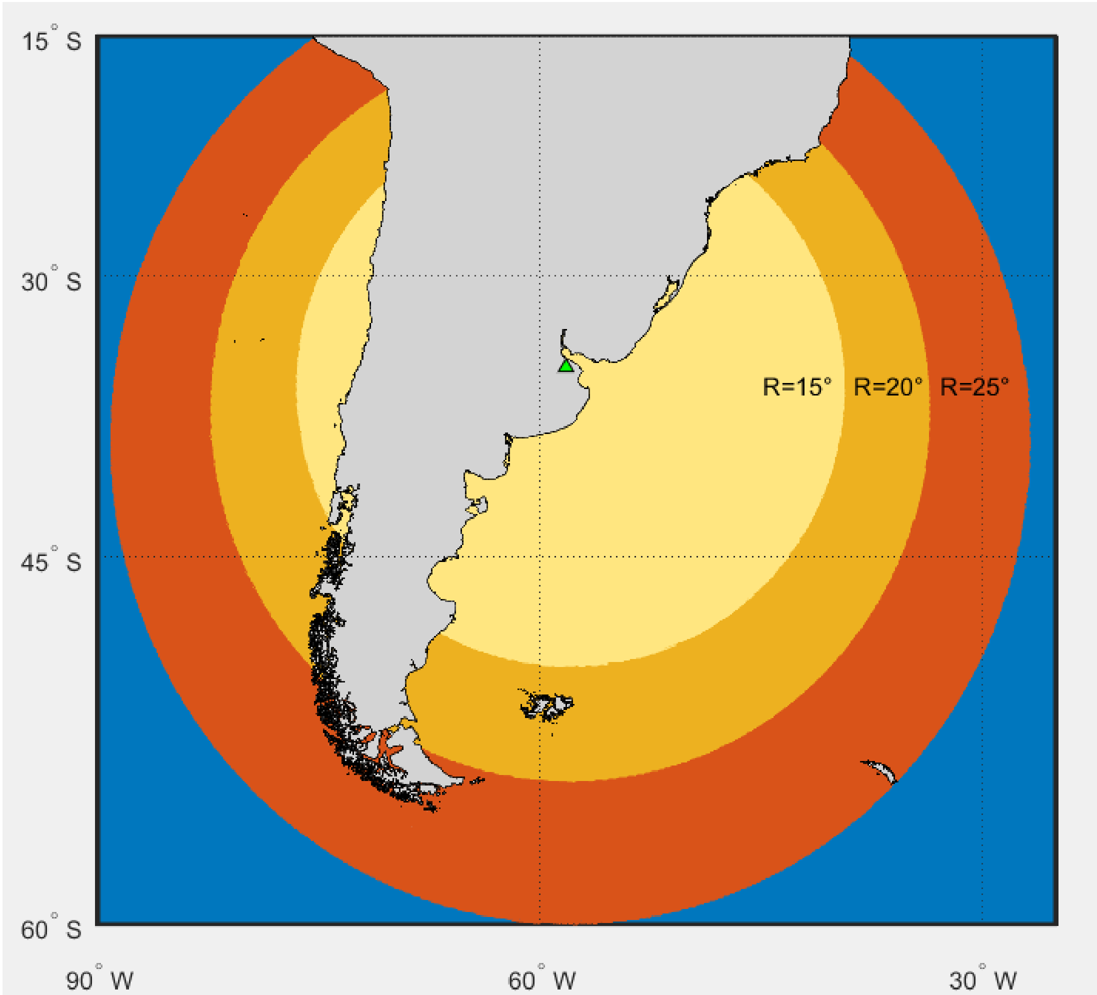

Figure 13. Map showing the increasing radial extent of the HR grid from 15° out to 25° from LPS. Note that only 3 subsets of the increments are shown for clarity. Actual increments ranged from 5° to the maximum extent of 39.9°. Green triangle: LPS location; colored circles: increasing radial extents of the HR grid; blue area: LR grid area; grey area: cells over South America not considered for loading. Note that the blue area changes with each step increase of the HR grid and is only shown on the outside for clarity.

Overlapping areas on the border between the HR and LR grids were recomputed upon every radial step increase of the HR grid. Figure 14 shows the net response at LPS with each 5° increment of the HR grid.

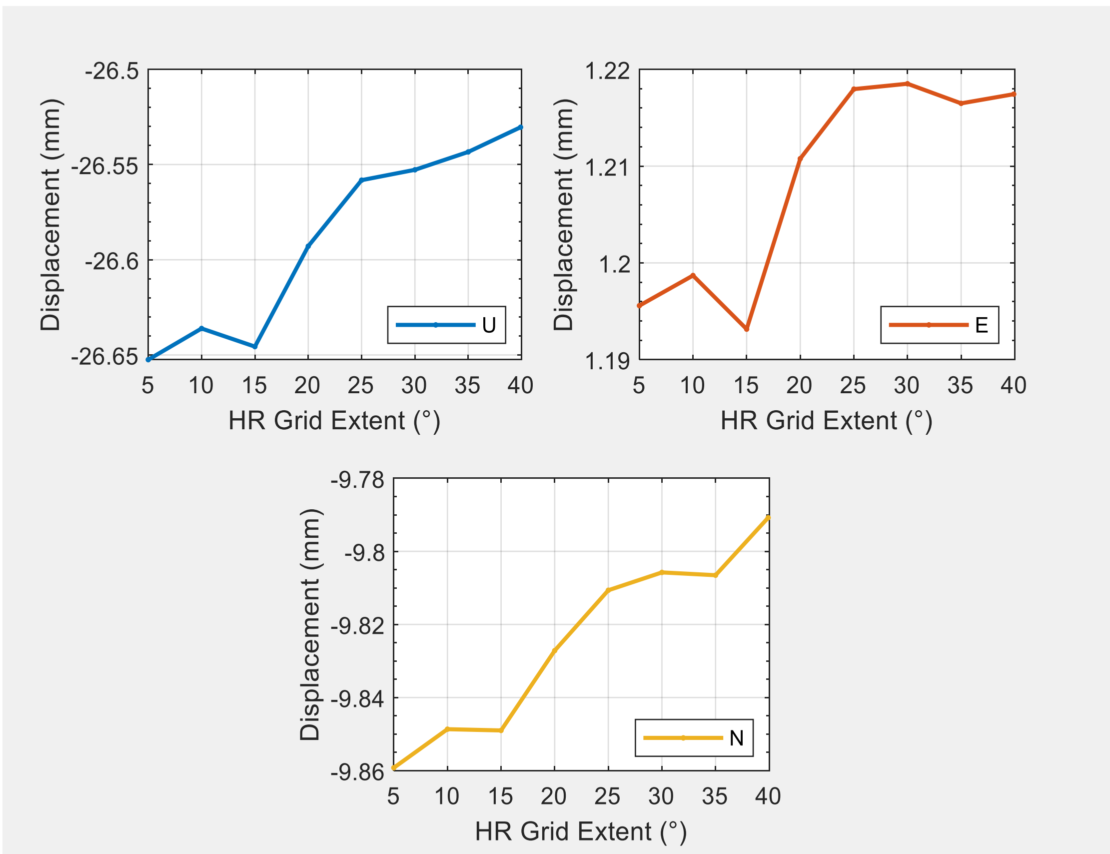


Figure 14. Net displacement at LPS with increasing extent of the HR grid in 5° increments and accounting for overlaps on grid borders.

Increasing extent of the HR grid generally led to smaller displacement magnitudes for *U* and *N* and larger magnitudes in the *E* component. This agrees with the notion that larger loads near the station yields greater magnitudes in displacement. Changes in displacements observed in Figure 14 directly agree with the increase or decrease in total water mass considered at each increment step of the HR grid (Figure 15). The expectation would be that the diminishing load from the LR grid would approximately equal the increase in load from the HR grid, however, this was not the case due to better coastline fit. The HR grid included more cells along the coasts of South America from 5° to 15° from LPS. The significant decreases in *U*, *N*, and total load after 15° highlights limitations of the LR grid near the complicated coastal geometry of South America below the 45° parallel, as well as the coarse coastline used for Antarctica in the LR grid. Correction for cells that should not be considered for tidal loading are left to interpolation of the OTM for the remainder of this study.

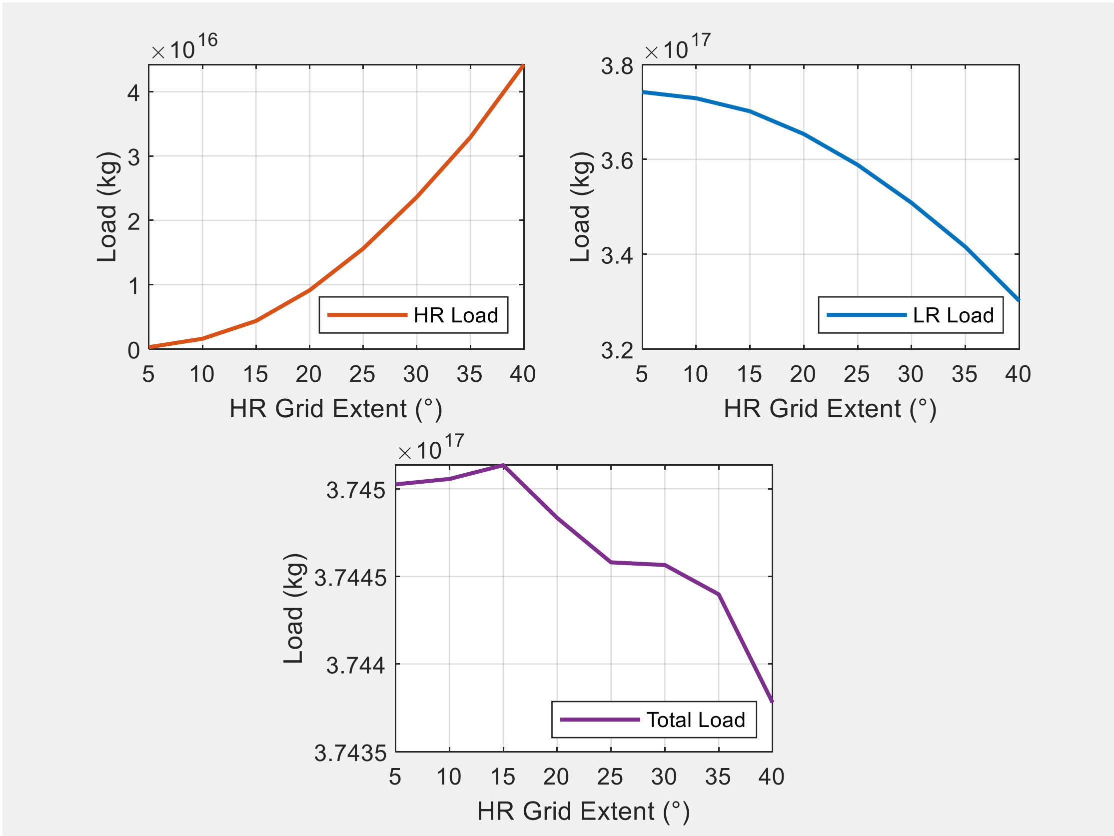

Figure 15. Sums of unit tidal mass considered at each increment of the HR grid. The total load is the sum between the HR and LR grid loads.

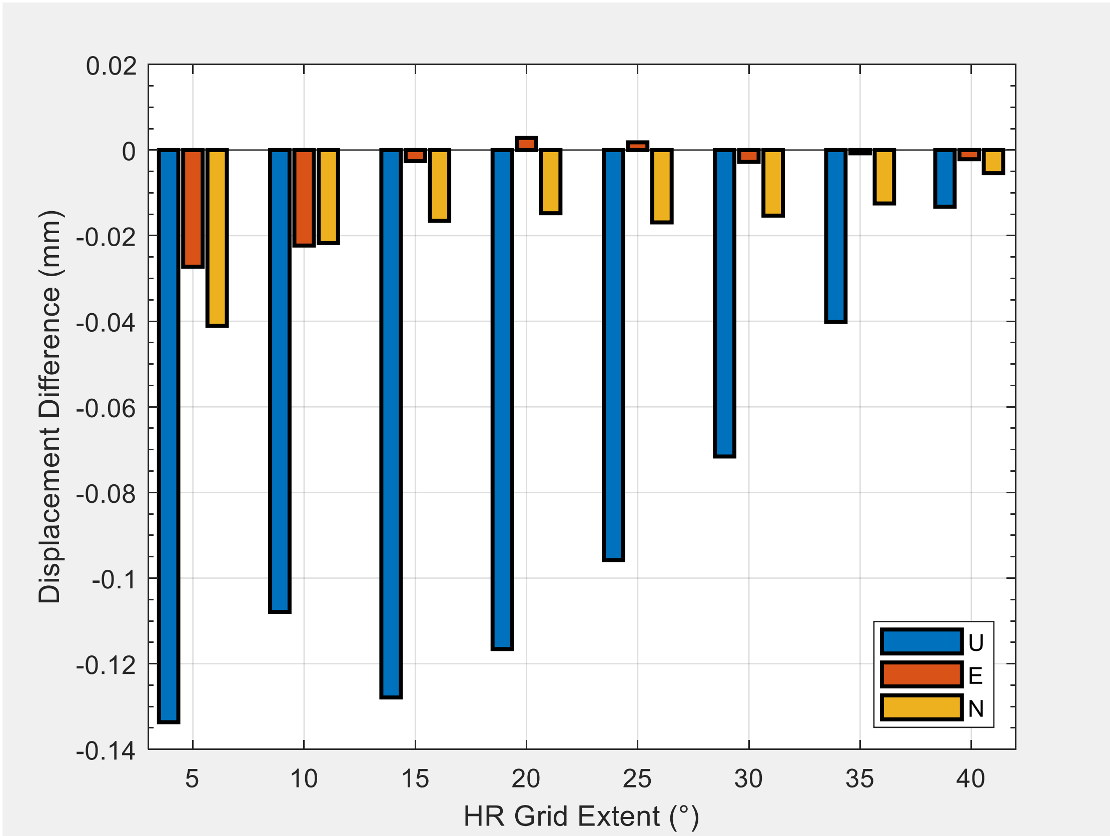

Figure 16. Differences in net displacement when accounting for cell overlaps versus neglecting the overlapping areas for each 5° increment of the HR grid extent.

In addition, results with and without treatment of border cells provides further insight for scaling the load by the fraction of water cover (Figure 16). The results aligned with the decay in LGF magnitudes with increasing distance. That is, accounting for cell overlaps became less important the farther the grid borders are from the station. Effects of overlap were insignificant at the maximum HR grid extent of 39.9° where differences in *U*, *E*, and *N* were -0.015, -0.002, and -0.007 mm, respectively. The same process was repeated except all LR cells within the bounds of the HR grid were masked out (Figure 17), meaning that small gaps between grids were present with no overlapping areas. The positive signs found in Figure 17 agree with initial expectations that gaps between the borders would generally underestimate ocean mass. However, the results of this test show that a degree of overlap is unnecessary if the high-resolution grid extends at least 20° from LPS. Similar results were found by masking out all LR cells within the HR2 grid, where net displacement differences amounted to 0.03, 0.005, and 0.01 mm for *U*, *E*, and *N*, respectively.

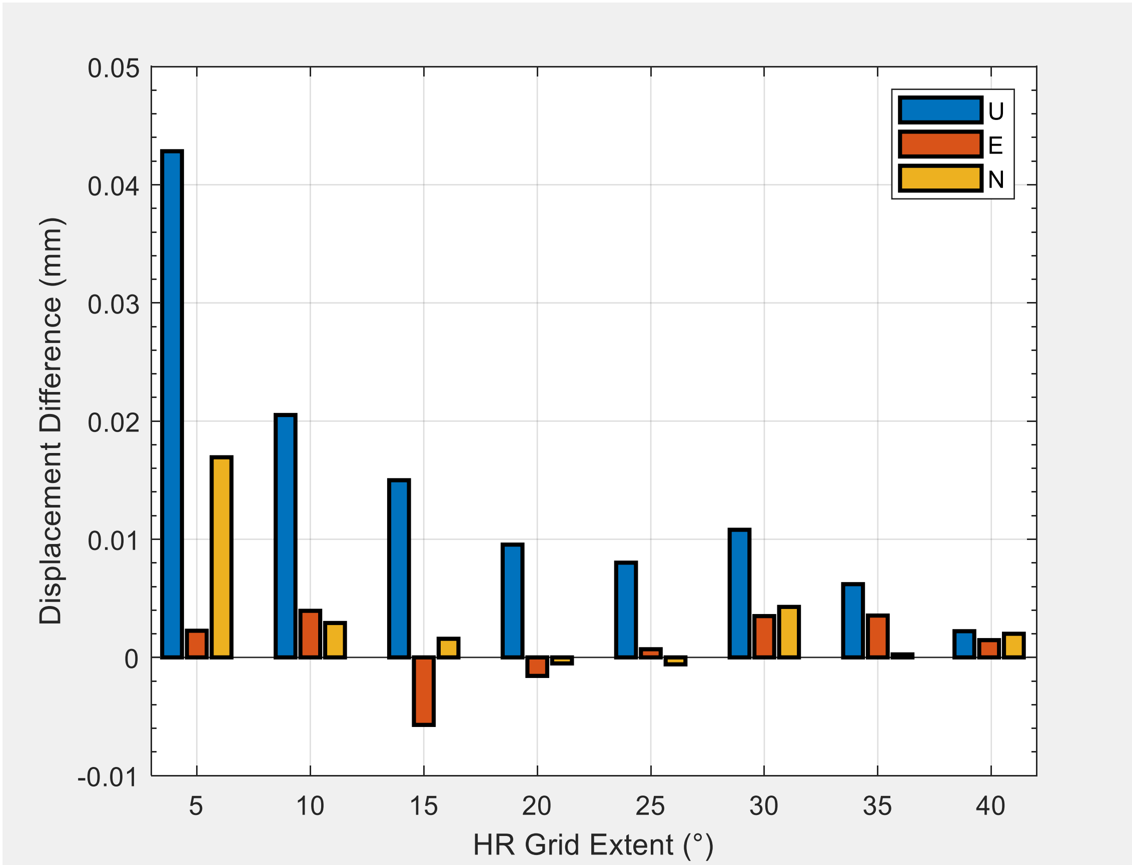

Figure 17. Differences in net displacement when including LR cells within 0.1° of the HR grid bounds and accounting for overlaps, versus masking out all LR cells within the bounds of the HR grid for each 5° increment of the HR grid.

The fraction of water method for treating coastal cells was found to be inadequate for small distances from the station. Insufficiency of this method stems from the distortion of where loading occurs along the coastline and the dependency on the cutoff value used to determine what cells are considered for loading. Changing the cutoff value for cells considered in the OTL calculations from 10% water cover to 50% water cover led to absolute changes of 0.163, 0.011, and 0.009 mm for *U*, *E*, and *N*, respectively. This significant change highlights the inconsistency of utilizing this method where approximately 80% of the differences originate from the near to medium field cells. However, scaling the load by $f_w$ may prove useful at larger distances where a HR grid cannot be afforded. As Figure 7 showed the importance of the far field, the impact of neglecting $f_w$ for coastal cells located greater than 45° from LPS was considered. In doing so, 7249 coastal cells were considered completely oceanic. Absolute differences in net displacements amounted to 0.0343, 0.0088, and 0.0252 mm for *U*, *E* and *N*, respectively. These small but noticeable differences can bring far field errors from other OTL programs to light. A higher-resolution LR grid combined with a higher-resolution global coastline could probe these errors further.

3.4 Model Comparisons

The EOT11a OTM was implemented with the MATLAB routine mainWithAdmittance that includes 18 major tidal harmonics with an additional 238 minor tides interpolated from admittance (Rieser et al., 2012). Obtained tidal heights were linearly interpolated to the disk model grids (HR+LR and HR2+LR combinations) over a span of 12 hours on 2 different dates: 08/12/2020, and 03/01/2021. The total response at LPS was computed by multiplying each row of the influence matrices, corresponding to the *U*, *E*, and *N* unit displacements from the $i^{th}$ disk, by the coinciding tidal heights for each 1-hour period over both dates. These dates were chosen based on the approximate start and end dates of this study and bear no practical significance. A period of 12 hours was chosen in attempt to capture most of the tidal signal in the estuary. Figure 18 shows interpolated tidal heights at each disk center (HR+LR grids) for a sample epoch. Although OTMs generally conserve mass themselves, deviations can be introduced upon interpolation. Mass was conserved by subtracting the average tidal height over the entire ocean area, rendering degree 0 loading effects negligible.

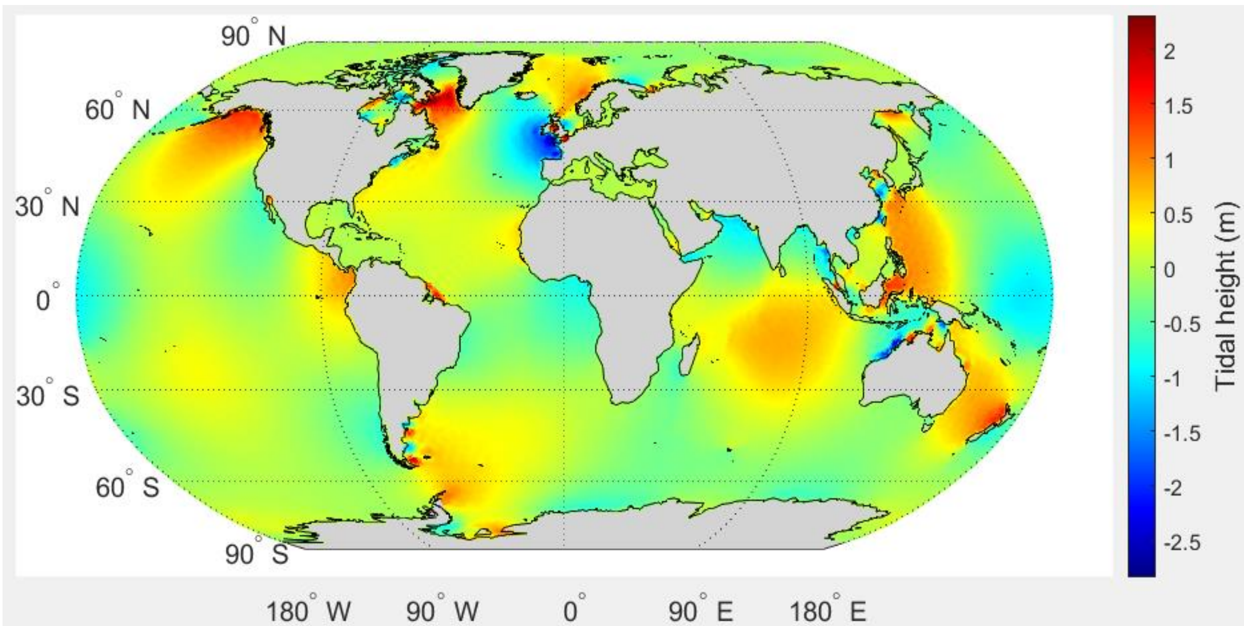


Figure 18. Tidal heights obtained from the EOT11a OTM and linearly interpolated to the HR+LR grid combination. Grey areas denote land with no tidal loading. Tidal heights shown correspond to March 1st, 2021 at 12 hours, 0 minutes, and 0 seconds. Map projection: Robinson.

Following the recommendations provided in the IERS Technical Note No. 36 (Gérard & Luzum, 2010), comparisons were made to the Ocean Tide Loading Provider for a rough check on our model accuracy. Site-specific tidal amplitudes and phases for LPS were computed via the Ocean Tide Loading Provider using the EOT11a OTM and elastic LGFs derived from the Gutenberg-Bullen A (GB) EM. This was also performed using viscoelastic LGFs based on the STW105 EM, also known as REF throughout this study. It should be noted that while REF and STW105 are considered the same EM, their names were kept separate to differentiate the REF used in this model and the STW105 from the Ocean Loading Provider. This was because the latter includes viscoelastic effects in the LGFs derived from STW105, while the LGFs for REF in our model were purely elastic.

The files obtained from the Ocean Loading Provider (computed with OLFG/OLMPP) were passed into the HARDISP function developed by Duncan Agnew to generate the displacement time series for the 12-hour period on both dates. HARDISP considers a total of 342 tidal constituents based on interpolation of admittance from 11 major tides (Gérard & Luzum, 2010). Comparisons were carried out between our model using PREM and the Ocean Loading Provider/HARDISP programs using GB, as well as our model using REF and the latter using STW105. Displacement predictions are shown for the PREM vs. GB model comparisons utilizing the HR+LR grid combination (Figures 19 and 20).

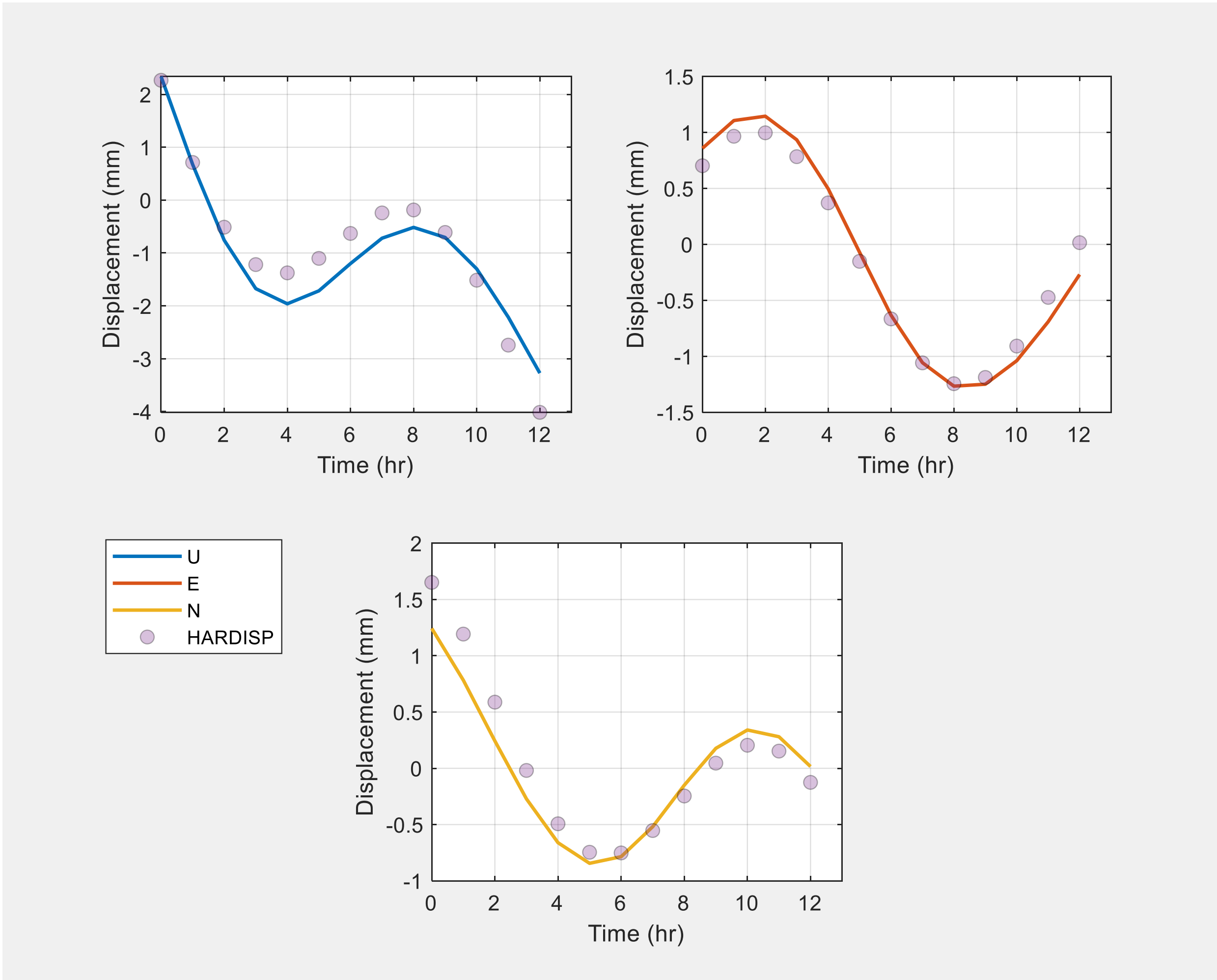


Figure 19. OTL predictions for August 12th, 2020 obtained from the disk load model (HR+LR grids) using the EM PREM, and from the Ocean Loading Provider/HARDISP using the EM GB.

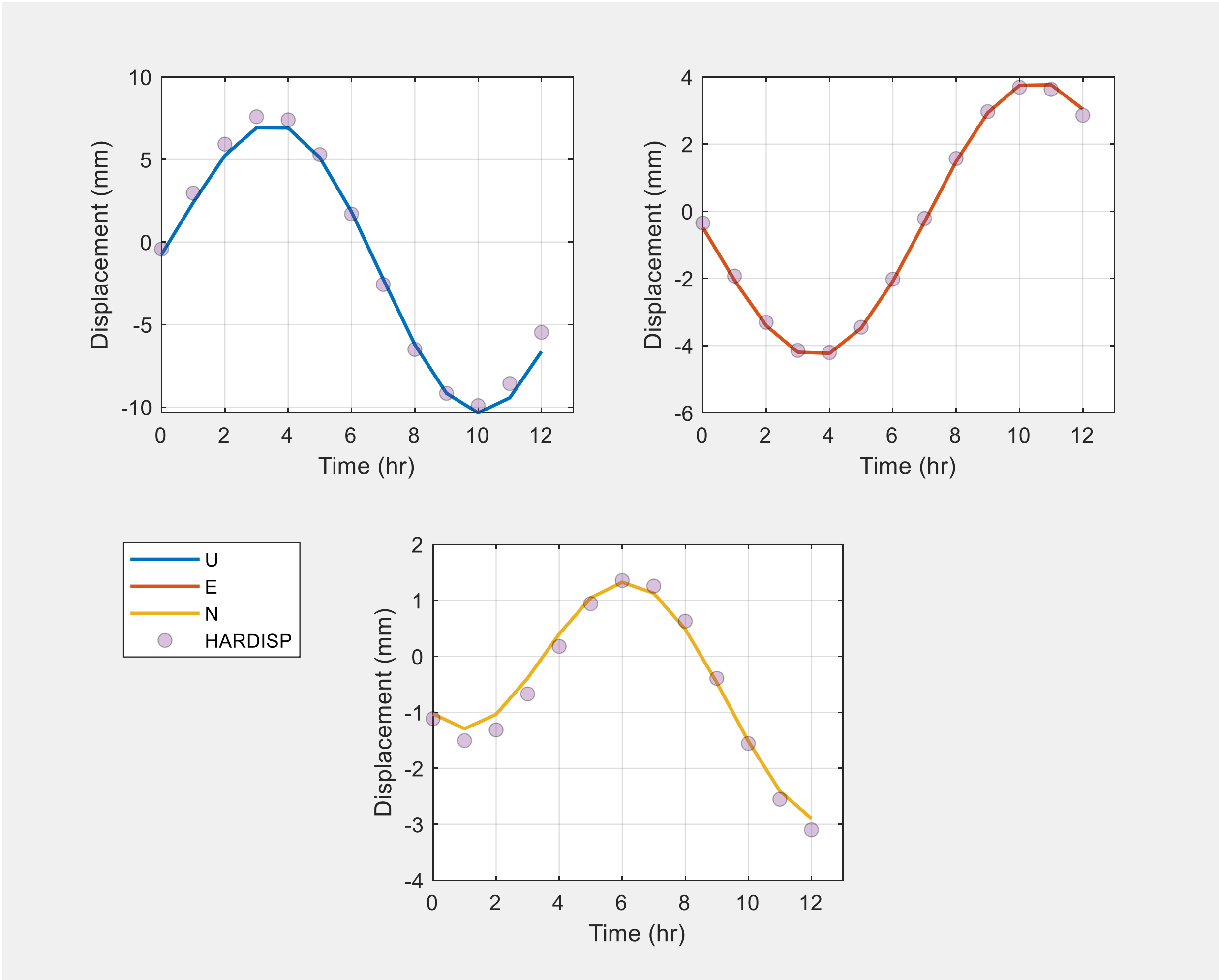


Figure 20. OTL predictions for March 1st, 2021 obtained from the disk load model (HR+LR grids) using the EM PREM, and from the Ocean Loading Provider/HARDISP programs using the EM GB.

Plots for the REF versus STW105 comparisons as well as the HR2+LR grid combination were similar to Figures 19 and 20 and are not shown here. Maximum differences for each displacement component, date, and model are highlighted in Table 3 for the HR+LR grid combination. Maximum differences in *U* occurred at the 12$^{th}$ hour mark across both dates and EMs and exceeded 1 mm only on the March 1$^{st}$ date. The REF vs. STW105 comparison led to slightly smaller maximum differences in all components for the August epochs, although generally larger maximum differences for the March epochs. Root mean square errors (RMSE) between our model and the Ocean Loading Provider/HARDISP for both EMs, epochs, and grid combinations are shown in Figure 21. The predictions obtained from the Ocean loading Provider were taken as the true values.

| | August 12th, 2020 | March 1st, 2021 |
|---|---|---|
| PREM Vs. GB | | |
| U (mm) | 0.743 (12) | 1.154 (12) |
| E (mm) | 0.284 (12) | 0.184 (12) |
| N (mm) | 0.413 (1) | 0.290 (3) |
| REF Vs. STW105 | | |
| U (mm) | 0.636 (12) | 1.215 (12) |
| E (mm) | 0.273 (2) | 0.435 (2) |
| N (mm) | 0.329 (1) | 0.270 (4) |

Table 3. Maximum differences between the diskload model (HR+LR grids) and Ocean Loading Provider/HARDISP programs for each displacement component and date. Terms in parenthesis represent the hour (0-12) for where the maximum difference occurred on the respective date.

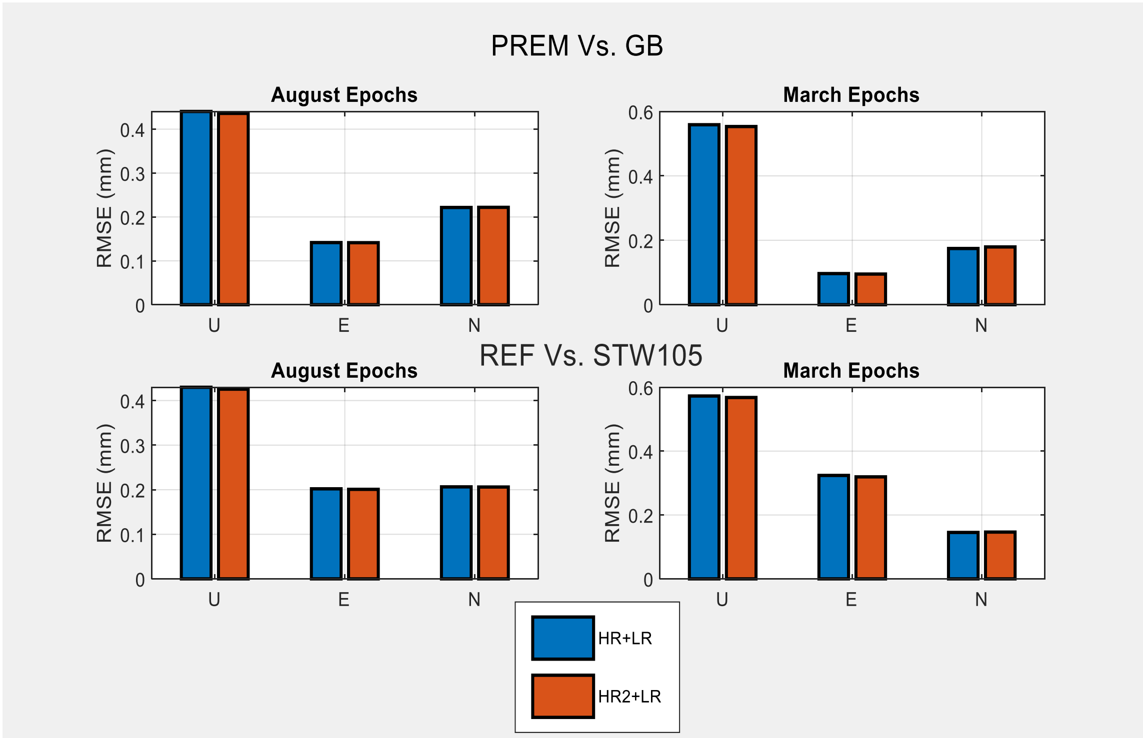

Figure 21. RMSEs for the model comparisons. Top row: RMSEs using our PREM and the GB EM from the Ocean Tide Loading Provider for *U*, *E*, and *N* over both dates considered. Bottom row: same as top row but for our REF and the Ocean Tide Loading Provider's STW105 EM.

Substituting the HR+LR grid combination with HR2+LR led to nearly identical results, indicating that the differences between our model and the Ocean Loading Provider/HARDISP programs largely stem from sources other than grid resolution in the near field. The RMSEs for the REF vs. STW105 comparison were less in the *N* component compared to PREM vs. GB, although higher in the *E* component across both dates. Nonetheless, obvious limitations to the model comparisons were present. Different EMs, LGFs, gridding and interpolation schemes, and tidal constituents considered inevitably produce variations in OTL predictions. Comparisons to other OTL programs was found to be necessary for more robust comparisons.

# Chapter 4. Discussion

This study simulated OTL displacements at LPS by utilizing the influence matrix technique with important insights gained on the sensitivity to EMs, gridding techniques, load sizes, and coastline resolutions for future development of OTL models here. The largest limitations on the efficiency of this model were the generation of grids, calculation of overlapping areas with land and border cells, and the choice of the OTM. Efficiencies in key steps of this model are discussed followed by important insights gained and necessary future improvements.

The adopted gridding technique proved inefficient with the computational resources available. This was largely due to the spherical tessellation program that required approximately 5 days for the LR grid and almost 9 days for the HR grid production. Several tests were conducted with modifications to the program with promising results; implementing parallel computing methods showed approximately 48 times faster grid generation times. Presumably, we will be able to achieve grid resolutions at finer scales with lower time requirements. Continual improvements are still being undertaken to optimize these methods for surface loading analyses. Nonetheless, this gridding method represents the best fit for disk load geometries and provides a solid framework for use in all types of surface loading studies. Equal area cells permitted spline fitting for markedly improved elastic calculation speeds, albeit at the cost of lengthy grid construction. This was done with nearly no loss in accuracy. The spline fitting, evaluation, and construction of the influence matrix for the HR+LR grid combination took an average of 4.27 seconds over 15 iterations. This is in comparison to 679 seconds required for the original diskload function to complete the same process.

Once the grids and influence matrices were established, the time required for estimating OTL displacements was largely dependent on the choice of the OTM and interpolation method. Running the EOT11a model followed by interpolation of tidal heights to the HR+LR grids took an average of 8.45 seconds over 15 iterations. However, this function is optimized for MATLAB and uses a maximum expansion degree of 120 (Rieser et al., 2012). Attempts at running the TPXO9 OTM by Egbert and Erofeeva (2002) via the Tidal Model Driver plugin for MATLAB proved much more time consuming. The TPXO9 model was not included for comparisons due to limited computational resources with frequent memory overloading.

Sensitivity to different EMs showed limitations of the diskload function for loads on a global scale. Mass conservation via the function was found to be deficient for OTL and had to be dealt with externally. Effects of degree 0 are thus unavoidably present and obvious in the unit response case when substituting various EMs. A difference of approximately 76% in net *U* displacement was found between PREM and REF for unit responses, whereas implementing the OTM with conserved mass reduced differences to ranges of 0.02% to 2.5%. These findings are consistent with previous studies (eg. Van Dam et al., 2003) showing that the choice of EM has noticeable, but relatively minor impact in practical application.

Using this gridding scheme introduced an additional error source due to the presumed grid stitching needed, or by simply leaving gaps in ocean area between the high-resolution and low-resolution grids. The negligible differences found between with and without accounting for overlapping cells at the HR extent of 39.9° represents a secure distance for the unit response case. However, masking out all LR cells in the HR grid bounds showed nearly identical results for an HR grid extent of at least 20° from LPS. This suggests that gaps in area are acceptable at this extent which eliminates the need for overlap calculations, greatly reducing the influence matrix generation time. To confidently do this, smaller LR grid cells with a higher-resolution coastline would likely be needed based on the reduction in total mass observed when incrementing the HR grid past 15°.

In addition, minor differences observed between the HR+LR and HR2+LR combinations when implementing the OTM show that the HR grid extent could be reduced even further. Reliance on the planar Voronoi tessellation may then be possible where even greater resolutions can be achieved at a mere fraction of the time required for the spherical tessellation. Based on the findings and methods used solely from this study, the distance for the high-resolution grid should be approximately 20° from LPS. However, a concrete recommendation for the resolution and extent of a high-resolution grid for the La Plata region cannot be given due to limited comparisons with other OTL programs. A thorough investigation on the effects of resolution and spatial extent for both the accuracy and computation speed would provide solid evidence to further support optimal grid parameters.

Based on the errors from using the coarse coastline in the near field (Figure 17), it is expected that using the coarse global coastline for the LR grid introduced a degree of error, although on an order much less than that observed near the station. These findings ultimately suggest that a higher global coastline resolution should be used in the LR grid for improved loading calculations. However, with the current disk size associated with the LR grid, the improvement in accuracy is expected to be negligible. Improving grid generation speeds will allow for smaller LR cells and can provide further insight into impacts of the far field.

Contributions from the estuary on net loading results proved to be small in the unit response case due to the small area and mass compared to the global oceans. Small tidal heights in the Rio de la Plata would further support results seen from the unit responses. Richter et. al (2017) showed that tidal amplitudes in the estuary typically reached only 2.5% of the open ocean. Similar results were found in this study when implementing the OTM: displacements in *U* from the estuary represented only 1.7% of the net displacement on average across the two dates considered. A key limitation here was the use of only a global OTM. Implementing a local tide model for the estuary is necessary for accurate OTL predictions (Richter et al., 2017). Future investigations can take an in-depth look at the regional tidal models available, e.g., the SEAT model (D'Onofrio et al., 2012), and implement more recent OTMs that provide higher resolution and improvements along other coastlines.

Comparisons between the Ocean Loading Provider and this model were made as a convenient check with differences expected. The agreement in sign and approximate magnitude of displacements between them show plausibility of the proposed disk load model. Penna et al. (2008) highlighted that differences between PREM LGFs of Francis and Mazzega (1990) and GB LGFs tabulated by Farrell (1972) led to differences in *U* of approximately 0.25 mm near coastlines. This could explain a significant percentage of the RMSEs for the comparison in this study. However, errors in *U* remained nearly constant across both EM comparisons. This may indicate a deeper problem in this model's convolution scheme and gridding process, or the number of tidal constituents included. The largest *U* differences all occurred at the 12$^{th}$ hour mark which leads to the notion that the discrepancy of tidal constituents included between models may play a significant role. Future testing can be done with other OTL programs with an emphasis on using the same EMs and OTMs for more precise comparisons. Additionally, isolating the main tidal constituents and their displacement impacts would provide a clear direction for sources of error.

# Chapter 5. Conclusion

The influence matrix technique for simulating OTL displacements at LPS led to a convenient framework for analyzing various effects of key model inputs. Errors introduced from the gridding and calculation scheme were enhanced in the near and medium fields when viewing unit responses, mainly due to the astronomical tides typically being smaller than 1 m for the estuary. Enlargement of these errors provides a solid basis for where improvements in this model need to be made. The HR grid was found to be an inadequate resolution for precise loading computations near the station, while the HR2 grid's spatial extent was not large enough to minimize coastline errors from the LR grid. Improvements in the LR grid resolution is also desired to provide a more complete view on the accuracy of far field impacts. Methods for dealing with coastal cells by utilizing the fraction of water cover could not be used in the near to medium fields based on the distortion of where tidal loading occurs. Settling this issue ultimately requires a higher-resolution grid that extends further ( > 5°) from LPS. Scaling the load by $f_w$ seems intuitively plausible for distances greater than 45°, however a higher-resolution grid in the far field is required to confirm this. The agreement in sign and approximate magnitude of OTL predictions between our model and the Ocean Tide Loading Provider shows a promising indication for future implementation.

Bibliography


Agnew, D. (2012). *SPOTL : Some Programs for Ocean- Tide Loading*.

Bevis, M., Melini, D., & Spada, G. (2016). On computing the geoelastic response to a disk load. *Geophysical Journal International*, *205*(3), 1804–1812. https://doi.org/10.1093/gji/ggw115

Blewitt, G. (2003). Self-consistency in reference frames, geocenter definition, and surface loading of the solid Earth. *Journal of Geophysical Research: Solid Earth*, *108*(B2). https://doi.org/10.1029/2002jb002082

Bos, M. S., & Baker, T. F. (2005). An estimate of the errors in gravity ocean tide loading computations. *Journal of Geodesy*, *79*(1–3), 50–63. https://doi.org/10.1007/s00190-005-0442-5

Bos, M. S., & Scherneck, H. (2013). *Computation of green's functions for ocean tide loading*.

Chen, J. Y., Pan, E., & Bevis, M. (2018). Accurate computation of the elastic load Love numbers to high spectral degree for a finely layered, transversely isotropic and self-gravitating Earth. *Geophysical Journal International*, *212*(2), 827–838. https://doi.org/10.1093/gji/ggx444

D'Onofrio, E., Oreiro, F., & Fiore, M. (2012). Simplified empirical astronomical tide model-An application for the Río de la Plata estuary. *Computers and Geosciences*, *44*, 196–202. https://doi.org/10.1016/j.cageo.2011.09.019

Dow, J. M., Neilan, R. E., & Rizos, C. (2009). The International GNSS Service in a changing landscape of Global Navigation Satellite Systems. *Journal of Geodesy*, *83*(3–4), 191–198. https://doi.org/10.1007/s00190-008-0300-3

Egbert, G. D., & Erofeeva, S. Y. (2002). Efficient inverse modeling of barotropic ocean tides. *Journal of Atmospheric and Oceanic Technology*, *19*(2), 183–204. https://doi.org/10.1175/1520-0426(2002)019<0183:EIMOBO>2.0.CO;2

Farrell, W. E. (1972). Deformation of the Earth by surface loads. *Reviews of Geophysics*, *10*(3), 761–797. https://doi.org/10.1029/RG010i003p00761

Fossati, M., & Piedra-Cueva, I. (2013). A 3D hydrodynamic numerical model of the Río de la Plata and Montevideo's coastal zone. *Applied Mathematical Modelling*, *37*(3), 1310–1332. https://doi.org/10.1016/j.apm.2012.04.010

Francis, O., & Mazzega, P. (1990). Global charts of ocean tide loading effects. *Journal of Geophysical Research*, *95*(C7), 11411. https://doi.org/10.1029/jc095ic07p11411

Gérard, P., & Luzum, B. (2010). IERS Conventions ( 2010 ). *Bureau International Des Poids Et Mesures Sevres (France)*, 1–179. http://www.iers.org/TN36/

Guo, J. Y., Li, Y. B., Huang, Y., Deng, H. T., Xu, S. Q., & Ning, J. S. (2004). Green's function of the deformation of the Earth as a result of atmospheric loading.

*Geophysical Journal International*, *159*(1), 53–68. https://doi.org/10.1111/j.1365-246X.2004.02410.x
Kustowski, B., Ekström, G., & Dziewoński, A. M. (2008). Anisotropic shear-wave velocity structure of the earth's mantle: A global model. *Journal of Geophysical Research: Solid Earth*, *113*(6), 1–23. https://doi.org/10.1029/2007JB005169
Martens, H. R., Rivera, L., & Simons, M. (2019). LoadDef: A Python-Based Toolkit to Model Elastic Deformation Caused by Surface Mass Loading on Spherically Symmetric Bodies. *Earth and Space Science*, *6*(2), 311–323. https://doi.org/10.1029/2018EA000462
Pan, E., Chen, J. Y., Bevis, M., Bordoni, A., Barletta, V. R., & Molavi Tabrizi, A. (2015). An analytical solution for the elastic response to surface loads imposed on a layered, transversely isotropic and self-gravitating Earth. *Geophysical Journal International*, *203*(3), 2150–2181. https://doi.org/10.1093/gji/ggv432
Penna, N. T., Bos, M. S., Baker, T. F., & Scherneck, H. G. (2008). Assessing the accuracy of predicted ocean tide loading displacement values. *Journal of Geodesy*, *82*(12), 893–907. https://doi.org/10.1007/s00190-008-0220-2
Piedra-Cueva, I., & Fossati, M. (2007). Residual currents and corridor of flow in the Rio de la Plata. *Applied Mathematical Modelling*, *31*(3), 564–577. https://doi.org/10.1016/j.apm.2005.11.033
Richter, A., Müller, L., Marderwald, E., Mendoza, L., Kruse, E., Perdomo, R., Scheinert, M., & Perdomo, S. (2017). Research Article. Towards a tidal loading model for the Argentine-German Geodetic Observatory (La Plata). *Journal of Geodetic Science*, *7*(1). https://doi.org/10.1515/jogs-2017-0002
Rieser, D., Mayer-Guerr Tr, T., Savcenko, R., Bosch, W., Wnsch, J., Dahle, C., & Flechtner, F. (2012). The ocean tide model EOT11a in spherical harmonics representation. *Technical Note*, *July*. url: http://portal. tugraz. at/portal/page/portal/Files/i5210/files/projekte/COTAGA/TN_EOT11a. pdf
Scherneck, H. (2016). *Encyclopedia of Geodesy*. https://doi.org/10.1007/978-3-319-02370-0
Shum, C. K., Woodworth, P. L., Andersen, B., Egbert, G. D., Francis, O., King, C., Klosko, S. M., Provost, C. Le, Li, X., Molines, J., Parke, M. E., Ray, R. D., Schlax, M. G., Tiemey, C. C., Vincent, P., & Wunsch, C. I. (1997). *102*(Cll).
Spada, G. (2003). *The theory behind TABOO Giorgio Spada*. 1–4.
Tegmark, M. (1996). An Icosahedron-based Method for Pixelizing the Celestial Sphere. *The Astrophysical Journal*, *470*(2), L81–L84. https://doi.org/10.1086/310310
Thomas, I. D., King, M. A., & Clarke, P. J. (2007). A comparison of GPS, VLBI and model estimates of ocean tide loading displacements. *Journal of Geodesy*, *81*(5), 359–368. https://doi.org/10.1007/s00190-006-0118-9
Van Dam, T. (2016). *Encyclopedia of Geodesy*. 1–5. https://doi.org/10.1007/978-3-319-02370-0
Van Dam, T., Plag, H.-P., Francis, O., & Gegout, P. (2003). GGFC Special Bureau for Loading: Current Status and Plans. *Proc.IERS Work.Comb..Res.Glob.Geophys.Fluids,IERS Tech.2003,30, 1998*(mm), 180–198.
Wessel, P., & Smith, W. H. F. (1996). A global, self-consistent, hierarchical, high-

resolution shoreline database. *Journal of Geophysical Research B: Solid Earth*, *101*(4), 8741–8743. https://doi.org/10.1029/96jb00104

Appendix A: All-Ocean World Displacements

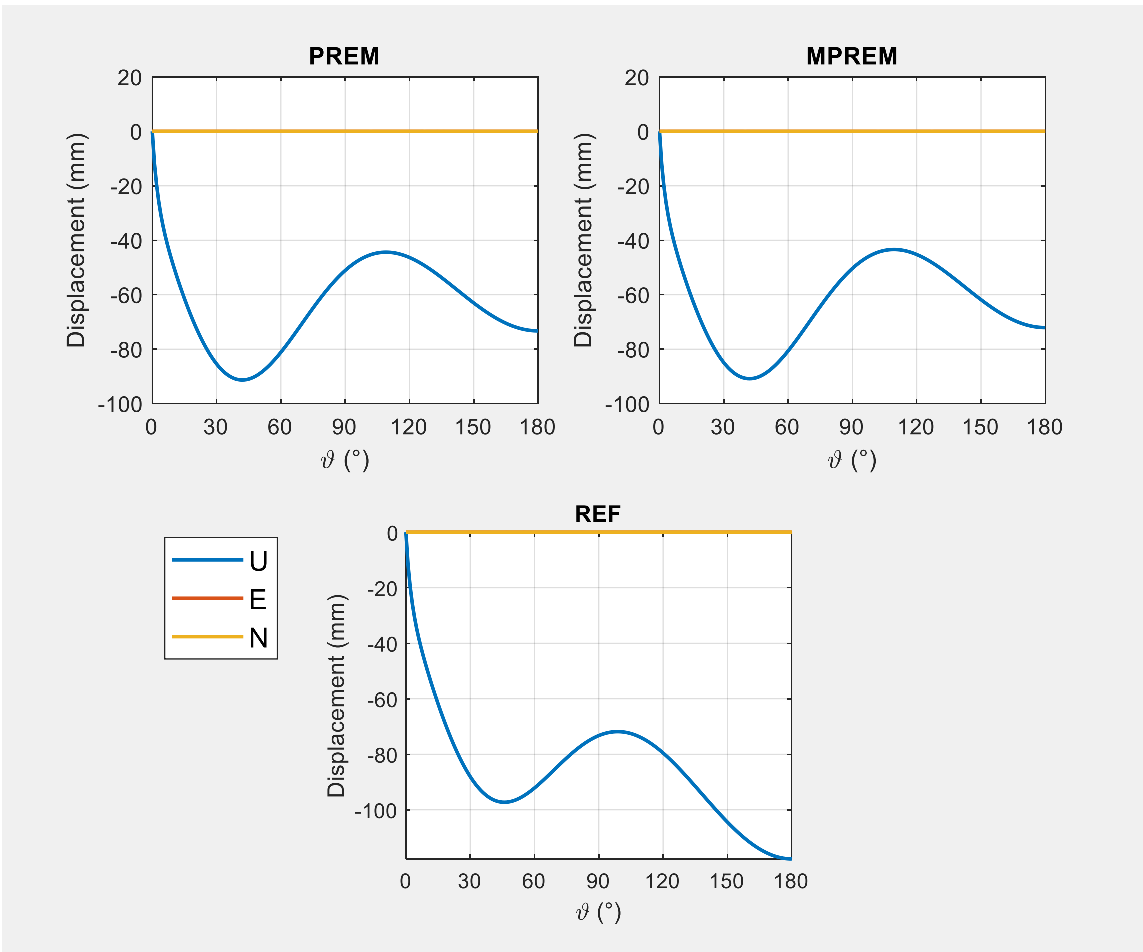


Figure 22. Cumulative Unit Response Displacements at LPS on an idealized all-ocean surface utilizing the HR+LR grid combination and with no mass conservation for the EMs PREM, MPREM, and REF. This is in contrast to Figure 6 that includes the presence of landmasses.